Topological susceptibility in finite temperature QCD with physical $(u/d,s,c)$ domain-wall quarks

Yu-Chih Chen,[1] Ting-Wai Chiu,[1,2,3,*] and Tung-Han Hsieh[4]

(TWQCD Collaboration)

[1]*Physics Department, National Taiwan University, Taipei, Taiwan 10617, Republic of China*
[2]*Institute of Physics, Academia Sinica, Taipei, Taiwan 11529, Republic of China*
[3]*Physics Department, National Taiwan Normal University, Taipei, Taiwan 11677, Republic of China*
[4]*Research Center for Applied Sciences, Academia Sinica, Taipei, Taiwan 11529, Republic of China*

(Received 4 April 2022; accepted 19 September 2022; published 11 October 2022)

We perform hybrid Monte-Carlo simulation of lattice QCD with $N_f = 2+1+1$ domain-wall quarks at the physical point, on the $64^3 \times (64, 20, 16, 12, 10, 8, 6)$ lattices, each with three lattice spacings. The lattice spacings and the bare quark masses are determined on the 64^4 lattices. The resulting gauge ensembles provide a basis for studying finite temperature QCD with $N_f = 2+1+1$ domain-wall quarks at the physical point. In this paper, we determine the topological susceptibility of the QCD vacuum for $T > T_c \sim 150$ MeV. The topological charge of each gauge configuration is measured by the clover charge in the Wilson flow at the same flow time in physical units, and the topological susceptibility $\chi_t(a,T)$ is determined for each ensemble with lattice spacing a and temperature T. Using the topological susceptibility $\chi_t(a,T)$ of 15 gauge ensembles with three lattice spacings and different temperatures in the range $T \sim 155$–516 MeV, we extract the topological susceptibility $\chi_t(T)$ in the continuum limit. To compare our results with others, we survey the continuum extrapolated $\chi_t(T)$ in lattice QCD with $N_f = 2+1(+1)$ dynamical quarks at/near the physical point and discuss their discrepancies. Moreover, a detailed discussion on the reweighting method for the domain-wall fermion is presented.

DOI: 10.1103/PhysRevD.106.074501

I. INTRODUCTION

The topological susceptibility χ_t is the most crucial quantity to measure the quantum fluctuations of the QCD vacuum, and it is defined as

$$\chi_t = \lim_{V\to\infty} \frac{\langle Q_t^2 \rangle}{V}, \tag{1}$$

where Q_t is the integer-valued topological charge of the gauge field in the four-dimensional volume V,

$$Q_t = \frac{g^2 \epsilon_{\mu\nu\lambda\sigma}}{32\pi^2} \int d^4x \, \mathrm{tr}[F_{\mu\nu}(x) F_{\lambda\sigma}(x)], \tag{2}$$

and $F_{\mu\nu} = T^a F^a_{\mu\nu}$ is the matrix-valued field tensor, with the normalization $\mathrm{tr}(T^a T^b) = \delta_{ab}/2$.

At low temperature $T < T_c \simeq 150$ MeV, χ_t is related to the chiral condensate Σ,

$$\Sigma = -\lim_{m_q\to 0} \lim_{V\to\infty} \frac{1}{\Omega} \int d^4x \, \langle \bar{q}(x) q(x) \rangle, \tag{3}$$

the order parameter of the spontaneously chiral symmetry breaking, and its nonzero value gives the majority of visible (nondark) mass in the present Universe.

For QCD with u and d light quarks, the chiral perturbation theory (ChPT) at the tree level gives the relation [1]

$$\chi_t = \Sigma \left(\frac{1}{m_u} + \frac{1}{m_d} \right)^{-1}, \tag{4}$$

which shows that χ_t is proportional to Σ. This implies that the nontrivial topological quantum fluctuations is the origin of the spontaneously chiral symmetry breaking. In other words, if χ_t is zero, then Σ is also zero, and the chiral symmetry is unbroken, and the mass of neutron/proton

*twchiu@phys.ntu.edu.tw

could be as light as ∼10 MeV rather than ∼940 MeV. Moreover, χ_t breaks the $U_A(1)$ symmetry and resolves the longstanding problem of why the flavor-singlet η' is much heavier than other nonsinglet (approximate) Goldstone bosons [2–4].

At finite temperature $T < T_c$, for small quark masses, the ChPT asserts that $\chi_t(T)$ is proportional to $\Sigma(T)$ and provides a prediction of $\chi_t(T)$ with the input $\chi_t(0)$ at zero temperature [5–8].

At temperature $T > T_c$, the chiral symmetry is restored, and $\Sigma(T) = 0$. However, it is unclear whether $U(1)_A$ is also restored at $T_1 \sim T_c$. Remarkably, if $U(1)_A$ is broken up to some $T_1 > T_c$ and restored for $T > T_1$, then there exists an interval (T_c, T_1) in which the nontrivial quantum fluctuations of the QCD vacuum can only make $\chi_t(T)$ nonzero but not $\Sigma(T)$. It is interesting to understand the physics underlying this mechanism.

Moreover, another interesting aspect of $\chi_t(T)$ is that it could play an important role in generating the majority of mass in the Universe, as a crucial input to the axion mass and energy density, a promising candidate for the dark matter in the Universe. The axion [9–11] is a pseudo-Nambu-Goldstone boson arising from the breaking of a hypothetical global chiral $U(1)$ extension of the Standard Model at an energy scale f_A much higher than the electroweak scale, the Pecci-Quinn mechanism. This not only solves the strong CP problem but also provides an explanation for the dark matter in the Universe. The axion mass at temperature T is proportional to $\sqrt{\chi_t(T)}$,

$$m_A(T) = \frac{\sqrt{\chi_t(T)}}{f_A}, \tag{5}$$

which is one of the key inputs to the equation of motion for the axion field evolving from the early Universe to the present one, with solutions predicting the relic axion energy density, through the misalignment mechanism [12–14].

In general, the determination of $\chi_t(T)$ requires nonperturbative approaches from the first principles of QCD. To this end, lattice QCD provides a viable nonperturbative determination of $\chi_t(T)$. Nevertheless, it becomes more and more challenging as the temperature gets higher and higher, since in principle the nontrivial configurations are more suppressed at higher temperatures, which in turn must require a much higher statistics in order to give a reliable determination. So far, direct simulations have only measured $\chi_t(T)$ up to $T \sim 550$ MeV. Nevertheless, for $T \gg T_c$, the temperature dependence of $\chi_t(T)$ can be obtained with the dilute instanton gas approximation (DIGA), which gives $\chi_t(T) \sim T^{-7-N_f/3}$ for N_f flavors of quarks [15].

Recent lattice studies of $\chi_t(T)$ aiming at the axion cosmology include various simulations with $N_f = 0$, $2+1$, and $2+1+1$, where the lattice fermions in the unquenched simulations include the staggered fermion, the Wilson fermion, and the Wilson twisted-mass fermion [16–22]. For recent reviews, see, e.g., Refs. [23,24] and references therein.

In this study, we perform the hybrid Monte Carlo (HMC) simulation of lattice QCD with $N_f = 2+1+1$ optimal domain-wall quarks at the physical point, on the $64^3 \times (64, 20, 16, 12, 10, 8, 6)$ lattices, each with three lattice spacings $a \sim (0.064, 0.068, 0.075)$ fm. The bare quark masses and lattice spacings are determined on the 64^4 lattices. The topological susceptibility of each gauge ensemble is measured by the Wilson flow at the flow time $t = 0.8192$ fm^2, with the clover definition for the topological charge Q_t. Using the topological susceptibility $\chi_t(a, T)$ of 15 gauge ensembles with three different lattice spacings and different temperatures in the range $T \sim 155$–516 MeV, we extract the topological susceptibility $\chi_t(T)$ in the continuum limit. Our preliminary results of $\chi_t(T)$ have been presented in lattice 2021 [25].

The outline of this paper is as follows. In Sec. II, we give a description of our HMC simulation with $N_f = 2+1+1$ domain-wall quarks at the physical point, including the actions, the algorithms, the gauge ensembles, the quark propagators, and the residual masses. In Sec. III, we describe our measurements of the topological susceptibility for our gauge ensembles, and the extrapolation to the continuum limit. In Sec. IV, we investigate the volume dependence of the topological susceptibility, by comparing the results between two spatial volumes $\sim(4\text{ fm})^3$ and $\sim(2\text{ fm})^3$, for $T \sim 190$–510 MeV. In Sec. V, we compare the topological charge/susceptibility of two different definitions: the index of the overlap Dirac operator versus the clover charge in the Wilson flow. In Sec. VI, we give a detailed discussion on the reweighting method for domain-wall fermion. In Sec. VII, we survey the continuum extrapolated topological susceptibility in recent lattice studies with $N_f = 2+1(+1)$ dynamical fermions at/near the physical point and discuss their discrepancies. In Sec. VIII, we conclude with some remarks. In Appendix A, we present our results of renormalized chiral condensate for $T \simeq 131$–516 MeV.

II. SIMULATION OF $N_f = 2+1+1$ LATTICE QCD WITH DOMAIN-WALL QUARKS

The first HMC simulation of $N_f = 2+1+1$ QCD with domain-wall quarks was performed on the $32^3 \times 64$ lattice with physical m_s and m_c, but unphysical $m_{u/d}$ with $M_\pi^\pm \sim 280$ MeV [26]. Later, the simulation was extended to physical $m_{u/d}$, m_s, and m_c on the 64^4 lattice, with $a \simeq 0.064$ fm, $L > 4$ fm, and $M_\pi L > 3$ [27,28]. Our present simulations with physical $(u/d, s, c)$ on the $64^3 \times (64, 20, 16, 12, 10, 8, 6) \equiv (N_x^3, N_t)$ lattices are extensions of our previous ones, using the same actions and algorithms and the same simulation code with tunings for the computational platform Nvidia DGX-V100. Most of our production runs were performed on 10–20 units of Nvidia DGX-V100

at two institutions in Taiwan, namely, Academia Sinica Grid Computing and National Center for High Performance Computing, from 2019 to 2021. Besides Nvidia DGX-V100, we also used other Nvidia GPU cards (e.g., RTX-2080Ti, GTX-1080Ti, GTX-TITAN-X, and GTX-1080) for HMC simulations on the $64^3 \times (12, 8, 6)$ lattices, which only require 8–22 GB device memory. In the following, we outline our HMC simulations of lattice QCD with $N_f = 2 + 1 + 1$ optimal domain-wall quarks at the physical point.

A. Lattice actions

For the gluon action, we use the Wilson plaquette action [29]

$$S_g(U) = \beta \sum_{\text{plaq.}} \left\{ 1 - \frac{1}{3} \text{ReTr}(U_p) \right\}, \tag{6}$$

where $\beta = 6/g_0^2$, and the boundary conditions of the link variables are periodic in all directions of the four-dimensional lattice. Then, setting β to three different values $\beta = \{6.15, 6.18, 6.20\}$ gives three different lattice spacings $a \simeq (0.075, 0.068, 0.064)$ fm, respectively. For each lattice spacing, the bare masses of $(m_{u/d}, m_s, m_c)$ are tuned such that the lowest-lying masses of the meson operators $\{\bar{u}\gamma_5 d, \bar{s}\gamma_i s, \bar{c}\gamma_i c\}$ are in good agreement with the physical masses of $\{\pi^{\pm}(140), \phi(1020), J/\psi(3097)\}$, respectively.

For the quark action, we use optimal domain-wall fermion (DWF) with the five-dimensional lattice fermion operator [30],

$$[\mathcal{D}(m_q)]_{xx';ss'}(m_q) = (\omega_s D_w + 1)_{xx'} \delta_{ss'} + (\omega_s D_w - 1)_{xx'} L_{ss'}, \tag{7}$$

where $\{\omega_s, s = 1, \ldots, N_s\}$ are given by the exact solution such that the effective four-dimensional lattice Dirac operator possesses optimal chiral symmetry for any finite N_s; i.e., the sign function $S_{N_s}(H_w)$ [see Eq. (13)] is exactly equal to the Zolotarev optimal rational approximation of $H_w/\sqrt{H_w^2}$. The indices x and x' denote the lattice sites on the four-dimensional lattice, s and s' denote the indices in the fifth dimension, and the Dirac and color indices have been suppressed. Here, D_w is the standard Wilson Dirac operator plus a negative parameter $-m_0$, which is fixed to -1.3 in our simulations,

$$(D_w)_{xx'} = (4 - m_0) - \frac{1}{2} \sum_{\hat{\mu}=1}^{4} [(1 - \gamma_\mu) U_\mu(x) \delta_{x+\hat{\mu},x'} + (1 + \gamma_\mu) U_\mu^\dagger(x') \delta_{x-\hat{\mu},x'}], \tag{8}$$

where $U_\mu(x)$ denotes the link variable pointing from x to $x + \hat{\mu}$. The boundary conditions of D_w on the four-dimensional lattice are periodic in space and antiperiodic in time. The operator L is independent of the gauge field, and it can be written as

$$L = P_+ L_+ + P_- L_-, \qquad P_\pm = (1 \pm \gamma_5)/2, \tag{9}$$

and

$$(L_+)_{ss'} = (L_-)_{s's} = \begin{cases} -(m_q/m_{PV})\delta_{N_s,s'}, & s = 1, \\ \delta_{s-1,s'}, & 1 < s \le N_s \end{cases}, \tag{10}$$

where m_q is the bare quark mass and $m_{PV} = 2m_0$ is the Pauli-Villars mass of optimal DWF. Note that the matrices $L_\pm$ satisfy $L_\pm^T = L_\mp$, and $R_5 L_\pm R_5 = L_\mp$, where R_5 is the reflection operator in the fifth dimension, with elements $(R_5)_{ss'} = \delta_{s',N_s+1-s}$. Thus, $R_5 L_\pm$ is real and symmetric.

Note that the Pauli-Villars mass m_{PV} is the upper cutoff for the quark mass m_q, since in the limit $m_q = m_{PV}$ the theory is reduced to the quenched approximation. Thus, any quark mass m_q is required to satisfy $m_q \ll m_{PV}$. Otherwise, the systematic error due to the mass cutoff is out of control. In general, the value of m_{PV} is $2m_0(1 - dm_0)$, where d is a parameter depending on the variant of DWF, e.g., $d = 0$ and $m_{PV} = 2m_0 < 4$ for optimal DWF and $d = 1/2$ and $m_{PV} = m_0(2 - m_0) < 1$ for the Shamir/Möbius DWF. Thus optimal DWF has the maximum value of $m_{PV} = 2m_0$, and it is theoretically the best choice for the simulation of lattice QCD with heavy c and b quarks; see Ref. [31] for further discussions.

The pseudofermion action for optimal DWF can be written as

$$S = \phi^\dagger \frac{\mathcal{D}(m_{PV})}{\mathcal{D}(m_q)} \phi, \qquad m_{PV} = 2m_0, \tag{11}$$

where ϕ and $\phi^\dagger$ are complex scalar fields carrying the same quantum numbers (color and spin) of the fermion fields. Integrating the pseudofermion fields in the fermionic partition function gives the fermion determinant of the effective four-dimensional lattice Dirac operator $D_{N_s}(m_q)$, i.e.,

$$\int [d\phi^\dagger][d\phi] \exp\left\{ -\phi^\dagger \frac{\mathcal{D}(m_{PV})}{\mathcal{D}(m_q)} \phi \right\} = \det \frac{\mathcal{D}(m_q)}{\mathcal{D}(m_{PV})} = \det D_{N_s}(m_q), \tag{12}$$

where

$$D_{N_s}(m_q) = m_q + \frac{1}{2}(m_{PV} - m_q)[1 + \gamma_5 S_{N_s}(H_w)], \; H_w = \gamma_5 D_w$$
$$S_{N_s}(H_w) = \frac{1 - \prod_{s=1}^{N_s} T_s}{1 + \prod_{s=1}^{N_s} T_s}, \quad T_s = \frac{1 - \omega_s H_w}{1 + \omega_s H_w}. \tag{13}$$

Note that the counterpart of Eq. (13) for Shamir/Möbius DWF can be obtained by replacing H_w with $H = \gamma_5 D_w(2 + D_w)^{-1}$, $m_{PV} = m_0(2 - m_0)$, and setting $\{\omega_s = 1, s = 1, \ldots, N_s\}$.

In the limit $N_s \to \infty$, $S_{N_s}(H_w) \to H_w/\sqrt{H_w^2}$, and $D_{N_s}(m_q)$ goes to

$$D_{\rm ov}(m_q) = m_q + \frac{1}{2}(m_{PV} - m_q)[1 + \gamma_5 S(H_w)],$$
$$S(H_w) \equiv \frac{H_w}{\sqrt{H_w^2}}. \tag{14}$$

In the massless limit $m_q = 0$, $D_{\rm ov}(0)$ is equal to the overlap-Dirac operator [32], and it satisfies the Ginsparg-Wilson relation [33]

$$D_{\rm ov}(0)\gamma_5 + \gamma_5 D_{\rm ov}(0) = \frac{2}{m_{PV}} D_{\rm ov}(0)\gamma_5 D_{\rm ov}(0)$$
$$\Leftrightarrow D_{\rm ov}^{-1}\gamma_5 + \gamma_5 D_{\rm ov}^{-1} = \frac{2}{m_{PV}}\gamma_5 1, \tag{15}$$

where the chiral symmetry is broken by a contact term, i.e., the exact chiral symmetry at finite lattice spacing.

For finite N_s, the exact chiral symmetry is broken, but optimal chiral symmetry can be attained if $S_{N_s}(H_w)$ is equal to the Zolotarev approximation of the sign function $H_w/\sqrt{H_w^2}$, which can be achieved by fixing $\{\omega_s\}$ according to the exact solution [30],

$$\omega_s = \frac{1}{\lambda_{\rm min}}\sqrt{1 - \kappa'^2 {\rm sn}^2(v_s;\kappa')}, \qquad s = 1, \ldots, N_s, \tag{16}$$

where ${\rm sn}(v_s;\kappa')$ is the Jacobian elliptic function with argument v_s and modulus $\kappa' = \sqrt{1 - \lambda_{\rm min}^2/\lambda_{\rm max}^2}$. Then, $S_{N_s}(H_w)$ is exactly equal to the Zolotarev optimal rational approximation of $H_w/\sqrt{H_w^2}$, i.e., the approximate sign function $S_{N_s}(H_w)$ satisfying the bound $|1 - S_{N_s}(\lambda)| \le d_Z$ for $\lambda^2 \in [\lambda_{\rm min}^2, \lambda_{\rm max}^2]$, where d_Z is the maximum deviation $|1 - \sqrt{x}R_Z(x)|_{\rm max}$ of the Zolotarev optimal rational polynomial $R_Z(x)$ of $1/\sqrt{x}$ for $x \in [1, \lambda_{\rm max}^2/\lambda_{\rm min}^2]$, with degree $(n-1, n)$ for $N_s = 2n$. The optimal weights (16) are used in our two-flavor simulation, with $N_s = 2n = 16$, $\lambda_{\rm min} = 0.05$, and $\lambda_{\rm max} = 6.2$, which gives the maximum deviation $d_Z \simeq 1.1944 \times 10^{-5}$.

For the simulation of one flavor, we used the exact one-flavor pseudofermion action for domain-wall fermion [34], which requires the weights $\{\omega_s\}$ satisfying the R_5 symmetry ($\omega_s = \omega_{N_s - s + 1}$). However, Eq. (16) does not satisfy the R_5 symmetry. The optimal $\{\omega_s\}$ satisfying R_5 symmetry are obtained in Ref. [35]. For $N_s = 2n$, it reads

$$\omega_s = \omega_{N_s+1-s} = \frac{1}{\lambda_{\rm min}}\sqrt{1 - \kappa'^2 {\rm sn}^2\left(\frac{(2s-1)K'}{N_s};\kappa'\right)},$$
$$s = 1, \ldots, N_s/2, \tag{17}$$

where ${\rm sn}(u;\kappa')$ is the Jacobian elliptic function with modulus $\kappa' = \sqrt{1 - \lambda_{\rm min}^2/\lambda_{\rm max}^2}$ and K' is the complete elliptic function of the first kind with modulus κ'. Then, the approximate sign function $S_{N_s}(H_w)$ satisfies the bound $0 \le 1 - S_{N_s}(\lambda) \le 2d_Z$ for $\lambda^2 \in [\lambda_{\rm min}^2, \lambda_{\rm max}^2]$, where d_Z is defined above. Note that in this case $\delta(\lambda) = 1 - S(\lambda)$ does not satisfy the criterion that the maxima and minima of $\delta(\lambda)$ all have the same magnitude but with the opposite sign ($\delta_{\rm min} = -\delta_{\rm max}$). However, the most salient features of optimal rational approximation of degree (m, n) are preserved; namely, the number of alternate maxima and minima is $(m + n + 2)$, with $(n + 1)$ maxima and $(m + 1)$ minima, and all maxima are equal to $2d_Z$, while all minima are equal to zero. This can be regarded as the generalized optimal rational approximation (with a constant shift). For our one-flavor simulation, setting $N_s = 2n = 16$, $\lambda_{\rm min} = 0.05$, and $\lambda_{\rm max} = 6.2$ gives the maximum deviation $2d_Z \simeq 2.3889 \times 10^{-5}$.

For domain-wall fermions, simulating $N_f = 2 + 1 + 1$ amounts to simulating $N_f = 2 + 2 + 1$ since

$$\left(\frac{\det \mathcal{D}(m_{u/d})}{\det \mathcal{D}(m_{PV})}\right)^2 \frac{\det \mathcal{D}(m_s)}{\det \mathcal{D}(m_{PV})}\frac{\det \mathcal{D}(m_c)}{\det \mathcal{D}(m_{PV})}$$
$$= \left(\frac{\det \mathcal{D}(m_{u/d})}{\det \mathcal{D}(m_{PV})}\right)^2 \left(\frac{\det \mathcal{D}(m_c)}{\det \mathcal{D}(m_{PV})}\right)^2 \frac{\det \mathcal{D}(m_s)}{\det \mathcal{D}(m_c)}. \tag{18}$$

Obviously, the simulation of two flavors with $(\det \mathcal{D}(m_c)/\det \mathcal{D}(m_{PV}))^2$ on the rhs of (18) is more efficient than its counterpart of one flavor with $\det \mathcal{D}(m_c)/\det \mathcal{D}(m_{PV})$ on the lhs. Moreover, the one-flavor simulation with $\det \mathcal{D}(m_s)/\det \mathcal{D}(m_c)$ on the rhs is more efficient than the one with $\det \mathcal{D}(m_s)/\det \mathcal{D}(m_{PV})$ on the lhs. Thus, we perform the HMC simulation with the expression on the rhs of Eq. (18).

For the two-flavor parts, $(\det \mathcal{D}(m_{u/d})/\det \mathcal{D}(m_{PV}))^2$ and $(\det \mathcal{D}(m_c)/\det \mathcal{D}(m_{PV}))^2$, we have implemented two options [36,37] for the $N_f = 2$ pseudofermion action in our code, and we have used the old action [36] in our present simulations. Note that both actions give consistent results in the HMC simulations. However, if $\lambda_{\rm min} \le 0.01$, the new action [37] is more efficient than the old one. For the old $N_f = 2$ pseudofermion action, it can be written as

$$S(m_q, m_{PV}) = \phi^\dagger C^\dagger(m_{PV})\{C(m_q)C^\dagger(m_q)\}^{-1}C(m_{PV})\phi,$$
$$m_{PV} = 2m_0, \tag{19}$$

where

$$C(m_q) = 1 - M_5(m_q) D_w^{\mathrm{OE}} M_5(m_q) D_w^{\mathrm{EO}},$$
$$M_5(m_q) = \{4 - m_0 + \omega^{-1/2}[1 - L(m_q)] \times [(1 + L(m_q)]^{-1}\omega^{-1/2}\}^{-1},$$

and $L(m_q)$ is defined in (9) and (10). Here, $\omega \equiv \mathrm{diag}\{\omega_1, \omega_2, \ldots, \omega_{N_s}\}$ is a diagonal matrix in the fifth dimension, and $D_w^{\mathrm{EO/OE}}$ denotes the part of D_w with gauge links pointing from even/odd sites to odd/even sites after even-odd preconditioning on the four-dimensional lattice. For the u/d quarks, mass preconditioning [38] is introduced with two levels of heavy masses: $m_{H_1} \sim 10 m_{u/d}$ and $m_{H_2} \sim 100 m_{u/d}$. Then, the $N_f = 2$ pseudofermion action $S(m_{u/d}, m_{PV})$ for u and d quarks is replaced with

$$\begin{aligned} &S(m_{u/d}, m_{H_1}) + S(m_{H_1}, m_{H_2}) + S(m_{H_2}, m_{PV}) \\ &= \phi^\dagger C^\dagger(m_{H_1})\{C(m_{u/d})C^\dagger(m_{u/d})\}^{-1} C(m_{H_1})\phi + \phi_1^\dagger C^\dagger(m_{H_2})\{C(m_{H_1})C^\dagger(m_{H_1})\}^{-1} C(m_{H_2})\phi_1 \\ &\quad + \phi_2^\dagger C^\dagger(m_{PV})\{C(m_{H_2})C^\dagger(m_{H_2})\}^{-1} C(m_{PV})\phi_2, \end{aligned}$$

which gives the partition function (fermion determinant) exactly the same as that of $S(m_{u/d}, m_{PV})$.

For the one-flavor part, $\det \mathcal{D}(m_s)/\det \mathcal{D}(m_c)$, we use the exact one-flavor pseudofermion action for domain-wall fermion [34]. For optimal DWF, it can be written as ($m_1 < m_2$)

$$\frac{\det \mathcal{D}(m_1)}{\det \mathcal{D}(m_2)} = \int d\phi_\pm^\dagger d\phi_\pm \exp\left(-\phi_+^\dagger G_+(m_1, m_2)\phi_+ - \phi_-^\dagger G_-(m_1, m_2)\phi_-\right), \tag{20}$$

where $\phi_\pm$ and $\phi_\pm^\dagger$ are pseudofermion fields (each with two spinor components) on the four-dimensional lattice. Here,

$$\begin{aligned} G_-(m_1, m_2) &= P_-\left[I - \left(\frac{m_2 - m_1}{m_2 + m_1}\right)\omega^{-1/2} v_-^T [H_T(m_1)]^{-1} v_- \omega^{-1/2}\right] P_-, \\ G_+(m_1, m_2) &= P_+\left[I + \left(\frac{m_2 - m_1}{m_2 + m_1}\right)\omega^{-1/2} v_+^T [H_T(m_2) - \Delta_+(m_1, m_2)P_+]^{-1} v_+ \omega^{-1/2}\right] P_+, \\ H_T(m_i) &= R_5\gamma_5[D_w + M(m_i)], \qquad i = 1, 2 \\ M(m_i) &= \omega^{-1/2}[1 - L(m_i)][1 + L(m_i)]^{-1}\omega^{-1/2}, \\ \Delta_\pm(m_1, m_2) &= \left(\frac{m_2 - m_1}{m_2 + m_1}\right)\omega^{-1/2} v_\pm v_\pm^T \omega^{-1/2}, \\ v_+^T &= (-1, 1, \ldots, (-1)^{N_s}), \\ v_- &= -v_+. \end{aligned}$$

B. Gauge ensembles

In the molecular dynamics, we use the Omelyan integrator [39] and the multiple-time scale method [40]. Setting the length of the HMC trajectory equal to 1, four different timescales are used for momentum updates, with the gauge force at level 0 and the fermion forces at levels 1/2/3, where the ratio of forces at levels 0/1/2/3 is ∼1:0.1:0.01:0.001. The step sizes for levels 0/1/2/3 are $1/(k_0k_1k_2k_3)$, $1/(k_1k_2k_3)$, $1/(k_2k_3)$, and $1/k_3$, where $(k_0, k_1, k_2, k_3) = (10, 2, 2, 12)$ is the most common setting in our simulations. The momentum updates with the two-flavor fermion forces corresponding to $S(m_{u/d}, m_{H_1})$, $S(m_{H_1}, m_{H_2})$, $S(m_{H_2}, m_{PV})$, and $S(m_c, m_{PV})$ are set to level 3, level 2, level 1, and level 1, respectively. The momentum updates with the one-flavor fermion forces corresponding to $\phi_+ G_+ \phi_+$ and $\phi_- G_- \phi_-$ are set to level 2 and level 3, respectively. With the smallest time interval $1/(k_0k_1k_2k_3)$, the numbers of momentum updates for levels 0/1/2/3 are $\{16k_0k_1k_2k_3 + 1, 8k_1k_2k_3 + 1, 4k_2k_3 + 1, 2k_3 + 1\}$, respectively, according to the Omelyan integrator. Our HMC code (DWFQCD) implements the entire HMC trajectory on GPUs, in which the most time-consuming parts of computing fermion forces and actions are obtained by solving very large and sparse linear systems via a conjugate gradient with mixed precision.

The initial thermalization of each ensemble was performed in one node with one to eight GPUs interconnected by the NVLink and/or PCIe bus. After thermalization, a set

TABLE I. The lattice parameters and statistics of the 15 gauge ensembles with $T > T_c$. The last three columns are the residual masses of u/d, s, and c quarks.

β	a (fm)	N_x	N_t	T (MeV)	N_{confs}	$(m_{u/d}a)_{\text{res}}$	$(m_s a)_{\text{res}}$	$(m_c a)_{\text{res}}$
6.20	0.0636	64	20	155	581	$2.39(56) \times 10^{-5}$	$1.92(53) \times 10^{-5}$	$7.59(38) \times 10^{-6}$
6.18	0.0685	64	16	180	650	$3.36(32) \times 10^{-5}$	$1.88(25) \times 10^{-5}$	$5.23(37) \times 10^{-6}$
6.20	0.0636	64	16	193	1577	$1.41(15) \times 10^{-5}$	$1.14(12) \times 10^{-5}$	$2.13(28) \times 10^{-6}$
6.15	0.0748	64	12	219	566	$3.16(84) \times 10^{-5}$	$2.70(85) \times 10^{-5}$	$1.24(31) \times 10^{-5}$
6.18	0.0685	64	12	240	500	$2.36(42) \times 10^{-5}$	$1.72(24) \times 10^{-5}$	$3.28(57) \times 10^{-6}$
6.20	0.0636	64	12	258	1373	$2.33(29) \times 10^{-5}$	$2.09(27) \times 10^{-5}$	$6.16(28) \times 10^{-6}$
6.15	0.0748	64	10	263	690	$2.38(36) \times 10^{-5}$	$1.98(29) \times 10^{-5}$	$7.51(26) \times 10^{-6}$
6.18	0.0685	64	10	288	665	$2.42(80) \times 10^{-5}$	$2.20(73) \times 10^{-5}$	$9.74(39) \times 10^{-6}$
6.20	0.0636	64	10	310	2547	$9.61(97) \times 10^{-6}$	$8.86(96) \times 10^{-6}$	$2.92(45) \times 10^{-6}$
6.15	0.0748	64	8	329	1581	$3.24(67) \times 10^{-5}$	$3.03(62) \times 10^{-5}$	$1.39(77) \times 10^{-5}$
6.18	0.0685	64	8	360	1822	$2.43(95) \times 10^{-5}$	$2.24(85) \times 10^{-5}$	$7.02(25) \times 10^{-6}$
6.20	0.0636	64	8	387	2665	$2.09(86) \times 10^{-5}$	$1.79(71) \times 10^{-5}$	$5.72(17) \times 10^{-6}$
6.15	0.0748	64	6	438	1714	$1.61(57) \times 10^{-5}$	$1.48(50) \times 10^{-5}$	$8.44(26) \times 10^{-6}$
6.18	0.0685	64	6	479	1983	$8.34(46) \times 10^{-6}$	$8.26(46) \times 10^{-6}$	$8.16(49) \times 10^{-6}$
6.20	0.0636	64	6	516	3038	$4.03(82) \times 10^{-6}$	$3.96(79) \times 10^{-6}$	$3.06(60) \times 10^{-6}$

of gauge configurations is sampled and distributed to 8–16 simulation units, and each unit performs an independent stream of HMC simulation. Here, one simulation unit consists of one to eight GPUs in one node, depending on the size of the device memory and the computational efficiency. Then, we sample one configuration every five trajectories in each stream and obtain a total number of configurations for each ensemble. The statistics of the 15 gauge ensembles with $T > T_c \sim 150$ MeV are listed in Table I, where $T = 1/(N_t a)$. For the gauge ensembles with $T < T_c$, some of them have not reached our desired statistics; thus, they will be presented in the future. For the ensemble of 64^4 at $\beta = 6.20$, preliminary results of topological susceptibility and the mass spectra of the low-lying mesons and baryons are presented in Ref. [28].

The lattice spacings and the bare quark masses at the physical point are determined on the 64^4 lattice, with $\{105, 110, 537\}$ configurations for $\beta = \{6.15, 6.18, 6.20\}$, respectively. For the determination of the lattice spacing, we use the Wilson flow [41,42] with the condition

$$\{t^2\langle E(t)\rangle\}|_{t=t_0} = 0.3,$$

to obtain $\sqrt{t_0}/a$, then use the input $\sqrt{t_0} = 0.1416(8)$ fm [43] to obtain the lattice spacing a. The lattice spacings for $\beta = \{6.15, 6.18, 6.20\}$ are listed in Table II. In all cases, the spatial volume satisfies $L^3 > (4\text{ fm})^3$ and $M_\pi L \gtrsim 3$.

For each lattice spacing, the bare quark masses of u/d, s, and c are tuned such that the lowest-lying masses of the meson operators $\{\bar{u}\gamma_5 d, \bar{s}\gamma_i s, \bar{c}\gamma_i c\}$ are in good agreement with the physical masses of $\{\pi^{\pm}(140), \phi(1020), J/\psi(3097)\}$. The bare quark masses of u/d, s, and c of each lattice spacing are listed in Table II.

C. Quark propagator

The valence quark propagator of the four-dimensional effective Dirac operator can be written as

$$(D_c + m_q)^{-1} = \left(1 - \frac{m_q}{2m_0}\right)^{-1}\left[D_{N_s}^{-1}(m_q) - \frac{1}{2m_0}\right],$$

where $D_{N_s}(m_q)$ is given in (13), and the mass and other parameters are exactly the same as those of the sea quark. The boundary conditions of the valence quark propagator are periodic in space and antiperiodic in time. To compute the valence quark propagator, we first solve the linear system with mixed-precision conjugate gradient algorithm, for the even-odd preconditioned $\mathcal{D}$ [44],

$$\mathcal{D}(m_q)|Y\rangle = \mathcal{D}(2m_0)B^{-1}|\text{source vector}\rangle, \tag{21}$$

where $B^{-1}_{x,s;x',s'} = \delta_{x,x'}(P_-\delta_{s,s'} + P_+\delta_{s+1,s'})$ with periodic boundary conditions in the fifth dimension. Then, the solution of (21) gives the valence quark propagator

$$(D_c + m_q)^{-1}_{x,x'} = (2m_0 - m_q)^{-1}[(BY)_{x,1;x',1} - \delta_{x,x'}]. \tag{22}$$

TABLE II. The lattice spacing and the quark masses of the $N_f = 2 + 1 + 1$ lattice QCD with optimal domain-wall quarks at the physical point.

β	a (fm)	$m_{u/d}a$	$m_s a$	$m_c a$
6.15	0.0748(1)	0.00200	0.064	0.705
6.18	0.0685(1)	0.00180	0.058	0.626
6.20	0.0636(1)	0.00125	0.040	0.550

D. Residual mass

To measure the chiral symmetry breaking due to finite N_s in DWF, we compute the residual mass according to the formula [45],

$$(m_q)_{\rm res} = \frac{\langle {\rm Tr}(D_c + m_q)^{-1}\rangle}{\langle {\rm Tr}[\gamma_5 (D_c + m_q)^{-1}\gamma_5 (D_c + m_q)^{-1}]\rangle} - m_q, \quad (23)$$

where Tr denotes the trace running over the site, color, and Dirac indices and the brackets $\langle\cdots\rangle$ denote the averaging over the configurations of the gauge ensemble. In the limit $N_s \to \infty$, D_c is exactly chiral symmetric, and the first term on the rhs of (23) is exactly equal to m_q; thus, the residual mass $(m_q)_{\rm res}$ is exactly zero, and the quark mass m_q is well defined for all gauge configurations. However, in practice, N_s is finite; thus, the residual mass is nonzero. To compute the numerator and the denominator of (23), we use 24–240 Z_2 noise vectors for each configuration to evaluate the all-to-all quark propagators. Alternatively, the numerator and the denominator of (23) can also be estimated with the quark propagator from one site (22), without summing over all sites. It turns out that both methods give consistent results; thus, we use their difference for the estimate of the systematic uncertainty of the residual mass. The residual masses of u/d, s, and c quarks for the 15 gauge ensembles with $T > T_c$ are listed in the last three columns of Table I, where the error bar combines both statistical and systematic uncertainties. The residual masses of u/d, s, and c quarks are less than 1.86%, 0.05%, and 0.002% of their bare masses, respectively. In units of MeV$/c^2$, the residual masses of u/d, s, and c quarks are less than 0.09, 0.08, and 0.04, respectively. This asserts that the chiral symmetry is well preserved such that the deviation of the bare quark mass m_q is sufficiently small in the effective four-dimensional Dirac operator $D_{N_s}(m_q)$ of optimal DWF, for both light and heavy quarks. In other words, the chiral symmetry in our simulations should be sufficiently precise to guarantee that the hadronic observables can be determined with a good precision, with the associated uncertainty much less than those due to statistics and other systematic ones.

III. TOPOLOGICAL CHARGE AND TOPOLOGICAL SUSCEPTIBILITY

On the lattice, the topological charge Q_t (2) is ill defined since we do not have $F_{\mu\nu}$ but only link variables. To extract $F_{\mu\nu}$ from the link variables is rather problematic, due to the strong short-distance fluctuation. The way to circumvent this problem is to smooth the link variables with smearing algorithms or the Wilson flow; then, it is possible to extract $F_{\mu\nu}(x)$ robustly from the smoothed gauge configuration. The resulting Q_t rounded to the nearest integer serves as a definition of the topological charge of this gauge configuration, and the topological susceptibility of a gauge ensemble can be measured.

For lattice QCD with exact chiral symmetry, the massless overlap Dirac operator in a nontrivial gauge background possesses exact zero modes with definite chirality, and its index satisfies the Atiyah-Singer index theorem $Q_t = n_+ - n_-$, where $n_\pm$ denotes the number of zero modes of $\pm$ chirality. Thus, one can project the zero modes of the overlap Dirac operator to obtain the index and also the topological charge, without smoothing the gauge configuration at all. Nevertheless, it is prohibitively expensive to project the zero modes of the overlap Dirac operator for our gauge ensembles with lattice sizes $64^3 \times (64, 20, 16, 12, 10, 8, 6)$. Thus, we use the Wilson flow to measure the topological susceptibility of each ensemble. Theoretically, the $\chi_t(a, T)$ by the Wilson flow is not necessarily equal to that using the index of overlap-Dirac operator. Nevertheless, both methods should give the same $\chi(T)$ in the continuum limit.

In this study, the topological charge Q_t of each configuration is measured by the Wilson flow, using the clover definition. The Wilson flow equation is integrated from the flow time $t/a^2 = 0$ to 256 with the step size 0.01. In Fig. 1, the fourth root of the topological susceptibility $a\chi_t^{1/4}(a, T)$ versus the flow time t/a^2 is plotted from $t/a^2 = 0$ to 256,

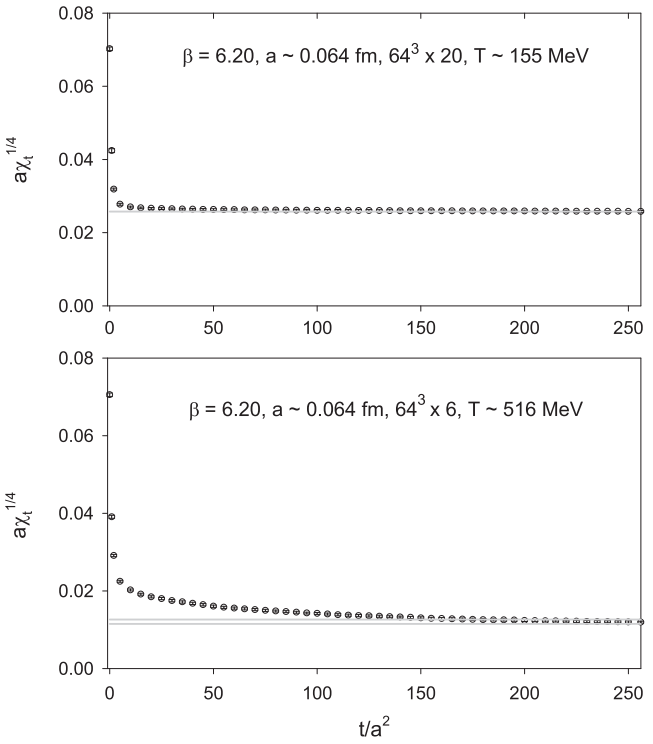

FIG. 1. The fourth root of the topological susceptibility $a\chi_t^{1/4}(T)$ vs the flow time t/a^2, for $T \sim 155$ MeV in the upper panel and $T \sim 516$ MeV in the lower panel. In each case, the plateau value of $a\chi_t^{1/4}$ is plotted as the horizontal line with the enveloping lines as the error bar.

TABLE III. The fourth root of the topological susceptibility $\chi_t^{1/4}(a,T)$ (in units of fm^{-1}) of the 15 gauge ensembles in this work, as a function of the lattice spacing a and the temperature T.

β	a (fm)	N_x	N_t	T (MeV)	N_{confs}	$\chi_t^{1/4}$ (fm^{-1})
6.20	0.0636	64	20	155	545	0.420(8)
6.18	0.0685	64	16	180	650	0.418(7)
6.20	0.0636	64	16	193	1577	0.417(5)
6.15	0.0748	64	12	219	566	0.425(9)
6.18	0.0685	64	12	240	500	0.403(7)
6.20	0.0636	64	12	258	1470	0.392(6)
6.15	0.0748	64	10	263	690	0.402(7)
6.18	0.0685	64	10	288	665	0.374(9)
6.20	0.0636	64	10	310	2547	0.358(4)
6.15	0.0748	64	8	329	1581	0.353(7)
6.18	0.0685	64	8	360	1822	0.320(5)
6.20	0.0636	64	8	387	2665	0.294(6)
6.15	0.0748	64	6	438	1714	0.254(6)
6.18	0.0685	64	6	479	1983	0.226(6)
6.20	0.0636	64	6	516	3038	0.202(7)

for $T \sim 155$ MeV (in the upper panel) and $T \sim 516$ MeV (in the lower panel). Evidently, as the temperature gets higher, $\chi_t(a,T)$ attains its plateau value at a larger flow time.

To extrapolate the topological susceptibility $\chi_t = \langle Q_t^2 \rangle / V$ to the continuum limit, Q_t is required to be measured at the same physical flow time for all lattice spacings, which is chosen to be 0.8192 fm^2 such that χ_t attains its plateau for all gauge ensembles in this study.

The results of the fourth root of the topological susceptibility $\chi_t^{1/4}(a,T)$ (in units of fm^{-1}) of 15 gauge ensembles are listed in the last column of Table III, where the error combines the statistical and the systematic ones. Here, the systematic error is estimated from the difference of $\chi_t^{1/4}(a,T)$ using two definitions Q_t, i.e., Q_{clover} and its nearest integer round$[Q_{\text{clover}}]$. The statistical error is estimated using the jackknife method with the bin size of which the statistical error saturates. The results of $\chi_t^{1/4}(a,T)$ of 15 gauge ensembles are plotted in Fig. 2. They are denoted by blue circles (for $a \sim 0.075$ fm), red inverted triangles (for $a \sim 0.068$ fm), and green squares (for $a \sim 0.064$ fm).

First, we observe that the five data points of $\chi_t^{1/4}(a,T)$ at high temperature $T > 350$ MeV can be fitted by the power law $\chi_t^{1/4}(T) \sim T^{-p}$, independent of the lattice spacing a. However, the power law cannot fit all 15 data points. To construct an analytic formula which can fit all data points of $\chi_t(T)$ for all temperatures, one considers a function which behaves like the power law $\sim (T_c/T)^p$ for $T \gg T_c$, but in general, it incorporates all higher-order corrections, i.e.,

$$\chi_t^{1/4}(T) = c_0 (T_c/T)^p \sum_{n=0} b_n (T_c/T)^n. \tag{24}$$

In practice, it is vital to recast (24) into a formula with fewer parameters, e.g.,

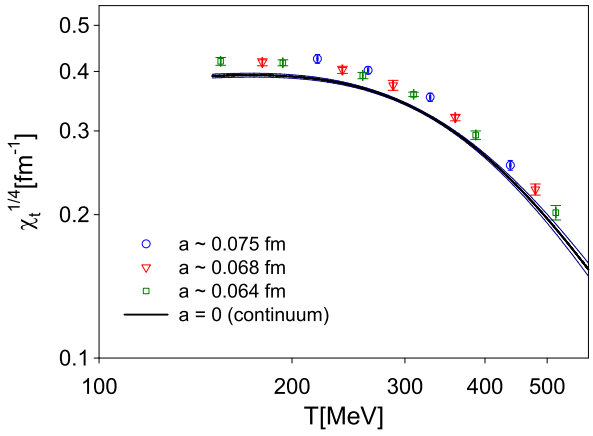

FIG. 2. The fourth root of topological susceptibility $\chi_t^{1/4}(a,T)$ vs the temperature T. The 15 data points with three different lattice spacings are denoted by blue circles ($a \sim 0.075$ fm), red inverted triangles ($a \sim 0.068$ fm), and green squares ($a \sim 0.064$ fm). The continuum limit resulting from fitting the 15 data points to the ansatz (26) is denoted by the black line, with the error bars as the enveloping blue lines.

$$\chi_t^{1/4}(T) = c_0 \frac{(T_c/T)^p}{1 + b_1(T_c/T) + b_2(T_c/T)^2}. \tag{25}$$

It turns out that the six data points of $\chi_t^{1/4}$ at $a \sim 0.064$ fm ($\beta = 6.20$) are well fitted by (25). Thus, for the global fitting of all $\chi_t^{1/4}(a,T)$ with different a and T, the simplest extension of (25) is to replace c_0 with $(c_0 + c_1 a^2)$. This leads to our ansatz

$$\chi_t^{1/4}(a,T) = (c_0 + c_1 a^2) \frac{(T_c/T)^p}{1 + b_1(T_c/T) + b_2(T_c/T)^2}, \quad T_c = 150 \text{ MeV}. \tag{26}$$

Fitting the 15 data points of $\chi_t^{1/4}$ in Table III to (26), it gives $c_0 = 1.89(3)$, $c_1 = 32.2(6.8)$, $p = 2.03(5)$, $b_1 = -2.42(19)$, and $b_2 = 6.25(14)$ with $\chi^2/\text{d.o.f.} = 0.21$. Note that the fitted value of the exponent p is rather insensitive to the choice of $T_c = 150$ MeV; i.e., any value of T_c in the range of 145–155 MeV gives almost the same value of p. Then, $\chi_t^{1/4}(T)$ in the continuum limit can be obtained by setting $a^2 = 0$ in (26), which is plotted as the solid black line in Fig. 2, with the error bars denoted by the enveloping blue solid lines. In the limit $T \gg T_c$, it becomes $\chi_t^{1/4}(T) = c_0 (T_c/T)^{2.03(5)}$, i.e., $\chi_t(T) = c_0^4 (T_c/T)^{8.1(2)}$, which agrees with the temperature dependence of $\chi_t(T)$ in the DIGA [15], i.e., $\chi_t(T) \sim T^{-8.3}$ for $N_f = 4$. This also implies that our data points of $\chi_t(a,T)$ for $T > 350$ MeV are valid, up to an overall constant factor.

It is interesting to note that our 15 data points of $\chi_t(a,T)$ are only up to the temperature $T \sim 515$ MeV. Nevertheless, they are sufficient to fix the coefficients of (26), which in turn can give $\chi_t(T)$ for any $T > T_c$. This is the major

advantage of having an analytic formula like (26). There are many possible variations of (26), e.g., replacing $(c_0 + c_1 a^2)$ with $(c_0 + c_1 a^2 + c_2 a^4)$, adding the a^2 term to the exponent p and/or the coefficients b_1 and b_2, etc. For our 15 data points, all variations give consistent results of $\chi_t(T)$ in the continuum limit.

IV. VOLUME DEPENDENCE OF THE TOPOLOGICAL SUSCEPTIBILITY

In this section, we investigate how χ_t changes with respect to the spatial volume. To this end, we performed HMC simulations of $N_f = 2+1+1$ lattice QCD on the $32^3 \times (64, 16, 12, 10, 8, 6)$ lattices at $\beta = 6.20$ with parameters and $(u/d, s, c)$ quark masses exactly the same as those in the HMC simulations on the $64^3 \times (64, 20, 16, 12, 10, 8, 6)$ lattices. For each HMC stream after thermalization, we sample one configuration every five trajectories and obtain the total number of configurations of each ensemble. The number of configurations of each ensemble with $T > T_c$ is given in the column with header $N_{\rm confs}$ in Table IV.

For the ensemble of lattice size $32^3 \times 64$ at $\beta = 6.20$, the total number of configurations is 187. Using the Wilson flow and the condition $\{t^2\langle E(t)\rangle\}|_{t=t_0} = 0.3$ with the input $\sqrt{t_0} = 0.1416(8)$ fm [43], we obtain the lattice spacing $a = 0.0641(1)$ fm. We also compute the quark propagators for u/d, s, and c quarks, and the time-correlation functions of the meson operators $\{\bar{u}\gamma_5 d, \bar{s}\gamma_i s, \bar{c}\gamma_i c\}$, and to extract the lowest-lying masses from the time-correlation functions. The resulting meson masses are in good agreement with the physical masses of $\pi^{\pm}(140)$, $\phi(1020)$, and $J/\psi(3097)$.

Similar to the $L/a = 64$ ensembles, the topological charge Q_t of each configuration in the $L/a = 32$ ensembles is measured by the clover definition in the Wilson flow. The Wilson flow equation is integrated from the flow time $t/a^2 = 0$ to 256 with the step size 0.01. The topological charge Q_t of each configuration is measured at the physical flow time 0.8192 fm^2, the same as that of any configuration in the $L/a = 64$ ensembles. The results of the fourth root of the topological susceptibility $\chi_t^{1/4}(a, T)$ (in units of fm^{-1}) of these five gauge ensembles are listed in the last column of Table IV, where the error combines the statistical and the systematic ones. Here, the systematic error is estimated from the difference of $\chi_t^{1/4}(a, T)$ using two definitions Q_t, i.e., $Q_{\rm clover}$ and its nearest integer round$[Q_{\rm clover}]$. The statistical error is estimated using the jackknife method with the bin size of which the statistical error saturates. Note that due to the lattice spacing $a = 0.0641(1)$ fm of the $L/a = 32$ ensembles being larger than $a = 0.0636(1)$ fm of the $L/a = 64$ ensembles, the temperature $T = 1/(N_t a)$ of the $L/a = 32$ ensemble in Table IV is slightly lower than that of the $L/a = 64$ ensemble with the same N_t (see Table III). Comparing the results of $\chi_t^{1/4}(a, T)$ in Table IV with the corresponding ones on the $64^3 \times (16, 12, 10, 8, 6)$ lattices in Table III, we see that those on the $32^3 \times (16, 12, 10, 8, 6)$ lattices are all slightly larger than the corresponding ones on the $64^3 \times (16, 12, 10, 8, 6)$ lattices, due to two different volumes as well as two slightly different temperatures. In Fig. 3, the results of $\chi_t^{1/4}(a, T)$ of the $L/a = 32$ ensembles are plotted as red triangles, while those of the $L/a = 64$ ensembles are plotted as black squares. Evidently, the volume dependence of $\chi_t^{1/4}(a, T)$ for two spatial volumes $(4.074\ \text{fm})^3$ and $(2.053\ \text{fm})^3$ is smaller than the uncertainty of $\chi_t^{1/4}(a, T)$ of the larger volume, for all ensembles with $T > 190$ MeV. Thus, it is expected that the infinite volume limit $(L/a \to \infty)$ of $\chi_t^{1/4}(a, T)$ would not be significantly different from its counterpart on the $L/a = 64$ lattice.

In general, the spatial volume dependence of χ_t (at fixed a and T) can be written as

$$\chi_t(L) = \chi_t(\infty)\left(1 + \sum_{n=1}^{\infty} c_n L^{-n}\right).$$

TABLE IV. The fourth root of the topological susceptibility $\chi_t^{1/4}(a, T)$ (in units of fm^{-1}) of five gauge ensembles with spatial size 32^3, as a function of the temperature $T = 1/(N_t a)$.

β	a (fm)	N_x	N_t	T (MeV)	$N_{\rm confs}$	$\chi_t^{1/4}$ (fm^{-1})
6.20	0.0641	32	16	192	1400	0.421(12)
6.20	0.0641	32	12	256	755	0.398(14)
6.20	0.0641	32	10	307	903	0.365(15)
6.20	0.0641	32	8	384	1208	0.296(13)
6.20	0.0641	32	6	512	1093	0.207(14)

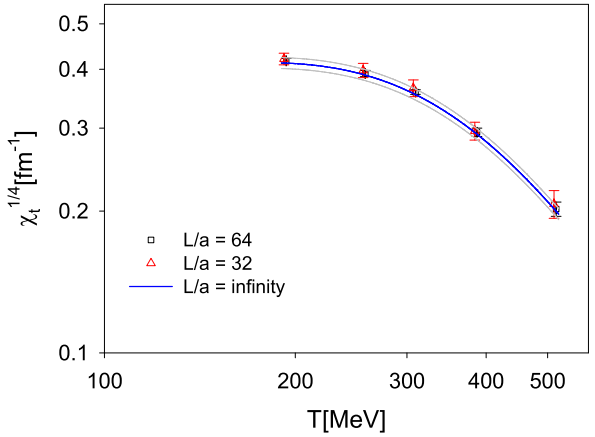

FIG. 3. The fourth root of topological susceptibility $\chi_t^{1/4}(a, T)$ vs the temperature T for $L/a = 32$ and $L/a = 64$ ensembles at $\beta = 6.20$. The five data points of the $L/a = 32$ ensembles are denoted by red triangles, while those of the $L/a = 64$ ensembles are denoted by black squares. The infinite volume limit resulting from fitting the ten data points to (27) is denoted by the blue line, with the error as the enveloping gray lines.

In practice, it is reasonable to replace the above expression with

$$\chi_t(L) = c_0 \exp(c_1/L), \qquad c_0 \equiv \chi_t(\infty),$$

and to determine c_0 and c_1 from the data of $\chi_t(L)$ with different volumes. Now, with two sets of $\chi_t^{1/4}(a,T)$ on two spatial volumes $(4.074\ \text{fm})^3$ and $(2.053\ \text{fm})^3$, we can extrapolate $\chi_t^{1/4}(a,T)$ to the infinite volume limit. Since each set of five data points of $\chi_t^{1/4}$ of $L/a = 32$ and $L/a = 64$ ensembles is well fitted by Eq. (25), it is natural to consider the ansatz

$$\chi_t^{1/4}(T,L) = c_0 \exp(c_1/L) \frac{(T_c/T)^p}{1 + b_1(T_c/T) + b_2(T_c/T)^2}, \quad T_c = 150\ \text{MeV}. \tag{27}$$

where c_0, c_1, p, b, and c are parameters and the dependence on the lattice spacing has been suppressed. In general, the dependence on the lattice spacing can be incorporated into (27), e.g., replacing c_0 with $(d_0 + d_1 a^2)$. The infinite volume limit resulting from fitting the ten data points to (27) is plotted as the blue line, with the error bar as the enveloping gray lines. Obviously, the $\chi_t(a,T)$ in the infinite volume limit is in good agreement with its counterparts of the $L/a = 64$ ensembles and the $L/a = 32$ ensembles.

For another two sets of $L/a = 64$ ensembles at $\beta = 6.18$ and $\beta = 6.15$, they have volumes $(4.384\ \text{fm})^3$ and $(4.787\ \text{fm})^3$, which are larger than the volume $(4.074\ \text{fm})^3$ of the $L/a = 64$ ensemble at $\beta = 6.20$; thus, it is expected that their finite-volume systematics are smaller than that of the $L/a = 64$ ensemble at $\beta = 6.20$. In other words, for all $L/a = 64$ ensembles in this study, the values of topological susceptibility do not suffer from significant finite-volume systematics.

V. COMPARISON WITH THE TOPOLOGICAL SUSCEPTIBILITY BY THE INDEX OF OVERLAP OPERATOR

In spite of the fact that our computer resources cannot afford to project the zero modes of the overlap operator for any one of the 15 gauge ensembles in this study, we can perform the overlap projections for a subset of an ensemble. Then, we can study to what extent the index $(n_+ - n_-)$ of the overlap operator agrees with Q_{clover} in the Wilson flow and also compare the $\chi_t(a,T)$ by the overlap index with that by the clover charge in the Wilson flow. To this end, we pick the ensemble of $64^3 \times 6$ lattice at $\beta = 6.20$, with $a \sim 0.0636$ fm and $T \sim 516$ MeV. From 1870 thermalized trajectories generated by the HMC simulation on one unit of Nvidia DGX-V100, we sample one configuration every five trajectories and obtain 374 configurations for the projection of the low modes of the overlap Dirac operator [46]. For these 374 configurations, the statistics of the overlap index $(n_+ - n_-)$ at $t = 0$ are given in the second column of Table V, together with those of round$[Q_{\text{clover}}]$ at $t/a^2 = 25$ (third column) and $t/a^2 = 256$ (fourth column) respectively.

TABLE V. The statistics of topological charge of 374 configurations on the $64^3 \times 6$ lattice at $T \sim 516$ MeV. The second column is the statistics of the overlap index $(n_+ - n_-)$ at $t = 0$. The third and the fourth columns are the statistics of the nearest integer of clover charge round$[Q_{\text{clover}}]$ at $t/a^2 = 25$ and 256, respectively.

		round$[Q_{\text{clover}}]$	
Q_t	$n_+ - n_-$	$t/a^2 = 25$	256
−2	3	0	0
−1	48	40	7
0	296	295	356
1	27	37	11
2	0	2	0

Using the overlap index, the topological susceptibility of these 374 configurations gives

$$a\chi_t^{1/4}(a,T)_{\text{overlap}} = 0.0195(8), \tag{28}$$

as shown by the horizontal red lines in Fig. 4. On the other hand, using round$[Q_{\text{clover}}]$ in the Wilson flow, the topological susceptibility attains the plateau for $t/a^2 \gtrsim 180$, and the plateau value gives

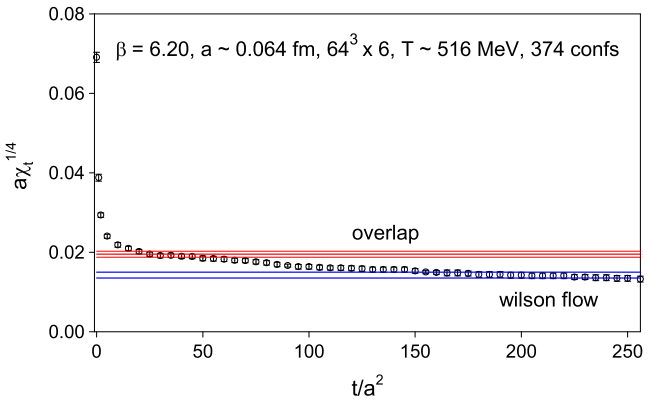

FIG. 4. The fourth root of the topological susceptibility $a\chi_t^{1/4}(a,T)$ of 374 configurations on the $64^3 \times 6$ lattice at $\beta = 6.20$, with $a \sim 0.0636$ fm and $T \sim 516$ MeV. The result of $a\chi_t^{1/4}$ by the overlap index for the 374 configurations at $t/a^2 = 0$ is denoted by the horizontal red lines, where the center line is the mean value and the upper and lower lines denote the statistical error which is estimated by the jackknife method with the bin size at which the statistical error saturates. The $a\chi_t^{1/4}$ by round$[Q_{\text{clover}}]$ in the Wilson flow is denoted by circles, and the plateau of $a\chi_t^{1/4}$ is denoted by the horizontal blue lines.

$$a\chi_t^{1/4}(a,T)_{\text{clover}} = 0.0143(8), \tag{29}$$

as shown by the horizontal blue lines in Fig. 4. Theoretically, one does not expect that (28) could be in good agreement with (29), since at high temperature such as $T \sim 516$ MeV the nontrivial topological fluctuations are highly suppressed; thus, it needs many more than 374 configurations in order to obtain reliable statistics for each topological sector. Here, we recall that in our previous study of $N_f = 2$ lattice QCD at zero temperature, for an ensemble of 535 configurations on the $24^3 \times 48$ lattice with $a \sim 0.06$ fm, we find that $a^4\chi_t(\text{overlap})$ at $t = 0$ is in good agreement with the plateau of $a^4\chi_t(\text{clover})$ in the Wilson flow [47]. Thus, we expect that if we could afford to compute the overlap index for the entire ensemble of ~3000 configurations on the $64^3 \times 6$ lattice at $\beta = 6.20$, then we may find that $a^4\chi_t(\text{overlap})$ at $t = 0$ could be in good agreement with the plateau of $a^4\chi_t(\text{clover})$ in the Wilson flow. Most importantly, the values in (28) and (29) are of the same order of magnitude. This seems to justify the plateau value of $\chi_t(\text{clover})$ in the Wilson flow, as well as the results of $\chi_t^{1/4}$ in Table III.

Note that at $t/a^2 = 25$ the topological susceptibility by round$[Q_{\text{clover}}]$ is

$$a\chi_t^{1/4}(a,T)_{\text{clover}}|_{t/a^2=25} = 0.0195(5), \tag{30}$$

which is equal to the $a\chi_t^{1/4}$ in (28) by the overlap index at $t = 0$. However, most of the nontrivial configurations according to round$[Q_{\text{clover}}] \neq 0$ do not coincide with those according to the overlap index with $(n_+ - n_-) \neq 0$ at $t = 0$, as shown by the vertical bar plot in Fig. 5. Among the 79 nontrivial configurations with round$[Q_{\text{clover}}] \neq 0$, there are only 11 configurations with round$[Q_{\text{clover}}]$ equal to the overlap index $(n_+ - n_-)$ at $t = 0$, 19 configurations satisfying $|\text{round}[Q_{\text{clover}}]| = |n_+ - n_-|$, and 22 configurations satisfying both round$[Q_{\text{clover}}] \neq 0$ and $(n_+ - n_-) \neq 0$. In other words, there are 57 nontrivial configurations according to round$[Q_{\text{clover}}] \neq 0$, but they are actually trivial configurations according to the overlap index at $t = 0$. Thus, for these 374 gauge configurations, even when χ_t measured by Q_{clover} at $t/a^2 = 25$ in the Wilson flow agrees with that by the overlap index at $t = 0$, there are ~72% (57 out of 79) of the nontrivial configurations with round$[Q_{\text{clover}}] \neq 0$ do not coincide with those with overlap index $(n_+ - n_-) \neq 0$. Obviously, such a discrepancy becomes larger at other Wilson flow time, where $\chi_t(\text{clover})$ is not equal to $\chi_t(\text{overlap})$ at $t = 0$. Moreover, we observe that such a discrepancy commonly exists in any gauge ensemble at zero/nonzero temperature.

For completeness, we also project 40 low modes of the overlap Dirac operator $D_{\text{ov}}(0)$ with the Wilson-flowed gauge configuration at $t/a^2 = 25$. We find that the overlap index is exactly equal to round$[Q_{\text{clover}}]$. Then, with the same Wilson-flowed gauge configuration at $t/a^2 = 25$, we repeat the projection for 40 low modes of the effective four-dimensional Dirac operator $D_{N_s}(0)$ of optimal DWF and find that the eigenvalues of its 40 low modes are almost exactly the same as those of the overlap operator $D_{\text{ov}}(0)$. Thus, its index is exactly equal to the overlap index and round$[Q_{\text{clover}}]$. Then, we repeat the same low-mode projections for several Wilson-flowed configurations at $t/a^2 > 25$ and find that for any one of these configurations the eigenvalues of 40 low modes of $D_{\text{ov}}(0)$ and $D_{N_s}(0)$ are almost exactly the same, and index$[D_{\text{ov}}(0)] =$ index$[D_{N_s}(0)] =$ round$[Q_{\text{clover}}]$. Thus, we conclude that the above equalities must hold for any Wilson-flowed configuration at $t/a^2 \geq 25$.

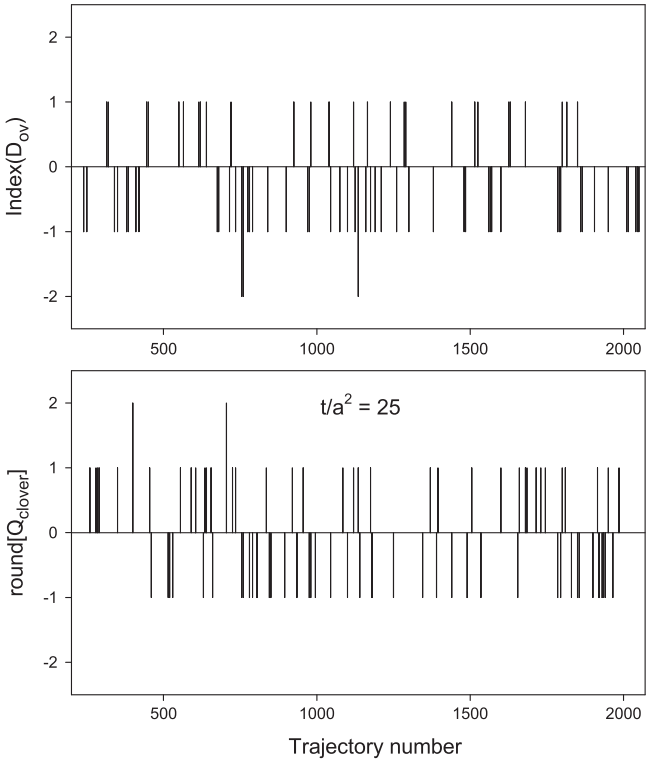

FIG. 5. The vertical bar plot of the overlap index (in the upper panel) and the round$[Q_{\text{clover}}]$ at $t/a^2 = 25$ in the Wilson flow (in the lower panel) for the 374 configurations (one configuration every five trajectories) on the $64^3 \times 6$ lattice at $T \sim 516$ MeV.

Note that the chiral symmetry in our simulation is not exact, with $N_s = 16$ and the optimal weights $\{\omega_s\}$ fixed by $\lambda_{\text{min}} = 0.05$ and $\lambda_{\text{max}} = 6.2$. Thus, the topological susceptibility in (28) is obtained by a mixed action with D_{ov} in the valence and D_{N_s} in the sea. The most concrete approach to resolve this issue is to perform HMC simulation in the exact chiral symmetry limit. For optimal DWF, the exact chiral symmetry limit is $N_s \to \infty$ and $\lambda_{\text{min}} \to 0$. This can be attained by increasing N_s and decreasing λ_{min} such that the systematic error due to the chiral symmetry breaking at finite lattice spacing becomes negligible in any physical

observables. For example, if taking $N_s = 32$, $\lambda_{\min} = 10^{-4}$, and $\lambda_{\max} = 6.2$, then the error of the sign function of H_w is less than 1.2×10^{-5} for eigenvalues of H_w satisfying $10^{-4} \le |\lambda(H_w)| \le 6.2$. Nevertheless, this set of simulations is estimated to be ~100 times more expensive than the present one, beyond the limit of our resources. In the next section, we examine the feasibility of using the reweighting method to correct this systematic error, without new simulations.

VI. REWEIGHTING METHOD

In this section, we discuss the reweighting method to correct the systematic error due to the DWF action in the HMC simulation not exactly chiral symmetric, without performing new simulations at all. Since the reweighting method deforms the path integral nonlocally, in principle, it is not guaranteed to give the correct result. Moreover, the reweighting method becomes inefficient if the weights have large fluctuations. In the following, we discuss the reweighting method for optimal DWF, which can be easily generalized to any DWF. At the end of this section, we also discuss the issue of using the clover charge in the Wilson flow to identify the nontrivial configurations in the reweighting method for nonchiral lattice Dirac operators (e.g., Wilson Dirac operator, staggered Dirac operator, etc.).

Consider a set of gauge configurations $\{U_i, i = 1, \ldots, N\}$ obtained by HMC simulation of lattice QCD with N_f domain-wall quarks, of which the effective four-dimensional Dirac operator is $D_{N_s}(m_q)$ in (13). In the exact chiral symmetry limit, $D_{N_s}(m_q)$ becomes $D_{\rm ov}(m_q)$. The reweighting method to obtain χ_t in the exact chiral symmetry limit amounts to computing

$$\chi_t^{\rm ov} = \frac{1}{V}\frac{\sum_{i=1}^N W_i Q_i^2}{\sum_{i=1}^N W_i} = \frac{1}{V}\frac{\sum_{Q_i \neq 0} W_i Q_i^2}{\sum_{i=1}^N W_i}, \tag{31}$$

where $Q_i = \text{index}\{D_{N_s}(0)[U_i]\}$, and

$$W_i = \prod_{j=1}^{N_f} \frac{\det D_{\rm ov}(m_j)[U_i]}{\det D_{N_s}(m_j)[U_i]}. \tag{32}$$

In general, for any observable $\mathcal{O}$ measured with $\{U_i\}$ from DWF simulation, its value in the exact chiral symmetry limit by the reweighting method is

$$\langle \mathcal{O} \rangle_{\rm ov} = \frac{\sum_{i=1}^N W_i \mathcal{O}_i}{\sum_{i=1}^N W_i}. \tag{33}$$

Note that in (31)–(33) $\{U_i\}$ are the gauge configurations without any smoothings, i.e., at the Wilson flow time $t = 0$. Otherwise, the results in (31)–(33) are not well defined, since they depend on how smooth the gauge configurations are. For example, consider the ensemble of 374 configurations on the $64^3 \times 6$ lattice as described in Sec. V. If one uses the Wilson-flowed gauge ensemble at any $t/a^2 \ge 25$ for the reweighting in (31)–(33), then $\text{index}[D_{N_s}(0)] = \text{index}[D_{\rm ov}(0)] = \text{round}[Q_{\rm clover}]$, and the weight factor $W_i = 1$ for all configurations in the ensemble. Consequently, the reweighted $\chi_t^{\rm ov}$ (31) in the exact chiral symmetry limit is the same as that measured by the index of $D_{N_s}(0)$, or $\text{round}[Q_{\rm clover}]$, i.e., $\chi_t^{\rm ov} = \chi_t^{\rm DWF} = \chi_t^{\rm clover}$, an incorrect result.

Since $\det D$ is equal to the product of all eigenvalues of D, $\det D_{\rm ov}(m_j)$ can be obtained for any m_j if all eigenvalues of $V_{\rm ov} \equiv \gamma_5 H_w/\sqrt{H_w^2}$ are known, i.e., from (14),

$$\lambda[D_{\rm ov}(m_j)] = m_j + \frac{1}{2}(m_{PV} - m_j)[1 + \lambda(V_{\rm ov})], \qquad V_{\rm ov} \equiv \gamma_5 H_w/\sqrt{H_w^2}. \tag{34}$$

Similarly, $\det D_{N_s}(m_j)$ can be obtained for any m_j if all eigenvalues of $V_{N_s} \equiv \gamma_5 S_{N_s}(H_w)$ are known,

$$\lambda[D_{N_s}(m_j)] = m_j + \frac{1}{2}(m_{PV} - m_j)[1 + \lambda(V_{N_s})], \qquad V_{N_s} \equiv \gamma_5 S_{N_s}(H_w), \tag{35}$$

where $S_{N_s}(H_w)$ for optimal DWF is defined in (13). Note that the counterparts of (34)–(35) for Shamir/Möbius DWF can be obtained by replacing H_w with $H = \gamma_5 D_w(2 + D_w)^{-1}$, $m_{PV} = m_0(2 - m_0)$ and setting $\{\omega_s = 1, s = 1, \ldots, N_s\}$ in $S_{N_s}(H)$. Since $V_{\rm ov}$ is unitary, its complex eigenvalues must come in conjugate pairs $\{e^{i\theta}, e^{-i\theta}\}$, with chirality $\phi^\dagger \gamma_5 \phi = 0$, where ϕ is the eigenvector. Its eigenmodes with real eigenvalues ± 1 must have chirality $+1$ or -1 and satisfy the chirality sum rule [48]

$$n_+ - n_- + N_+ - N_- = 0, \tag{36}$$

where $n_\pm$ denotes the number of eigenmodes with eigenvalue -1 and chirality ± 1 and $N_\pm$ denotes the number of eigenmodes with eigenvalue $+1$ and chirality ± 1. Empirically, the real eigenmodes always satisfy either ($n_+ = N_-$ and $n_- = N_+ = 0$) or ($n_- = N_+$ and $n_+ = N_- = 0$). According to (34), the -1 eigenmodes of $V_{\rm ov}$ correspond to the zero mode of $D_{\rm ov}(0)$, and the $+1$ eigenmodes of $V_{\rm ov}$ correspond to the nonzero real eigenmodes of $D_{\rm ov}(0)$ with eigenvalue m_{PV}, where $m_{PV} = 2m_0$ for optimal DWF. Thus, each zero mode of $D_{\rm ov}(0)$ with definite chirality ± 1 must be accompanied with a nonzero real eigenmode at $2m_0$ with opposite chirality ∓ 1. For V_{N_s} in optimal DWF, it is not exactly unitary, but it is sufficiently close to unitary such that its eigenvalues are almost the same as those of $V_{\rm ov}$ except the real eigenmodes

at ± 1. In other words, the major difference between the eigenvalues of $D_{\rm ov}(0)$ and $D_{N_s}(0)$ are the number of zero modes and the nonzero real eigenmodes at $2m_0$. In the following, we consider all possibilities for the zero modes of $D_{\rm ov}(0)$ and $D_{N_s}(0)$:

(1) Both $D_{\rm ov}(0)$ and $D_{N_s}(0)$ do not have any zero modes. In this case, both $V_{\rm ov}$ and V_{N_s} do not have ± 1 real eigenmodes but only have complex conjugate pairs which are almost identical for both operators. Thus, according to (34) and (35), the weight factor (32) is

$$W^{(1)} \simeq 1. \tag{37}$$

(2) Both $D_{\rm ov}(0)$ and $D_{N_s}(0)$ have $n = n_+ + n_-$ zero modes ($n \geq 1$). In this case, both $V_{\rm ov}$ and V_{N_s} have n pairs of real eigenvalues at $+1$ and -1. But the -1 eigenvalues of V_{N_s} could have small deviations, say, $-1+\epsilon_k, k = 1, \ldots, n$, where the size of ϵ_k depends on how good $S_{N_s}(H_w)$ can approximate the sign function $H_w/\sqrt{H_w^2}$, especially in the low-lying spectrum of $|H_w|$, i.e., how small the $\lambda_{\rm min}$ for computing the weights $\{\omega_s\}$ in optimal DWF is. The complex conjugate pairs are almost identical for both $V_{\rm ov}$ and V_{N_s}. Then, according to (34) and (35), the weight factor (32) for $N_f = 2+1+1$ QCD is

$$W^{(2)} = \prod_{k=1}^{n} \left[\frac{m_{u/d}}{m_{u/d} + \epsilon_k(m_0 - m_{u/d}/2)}\right]^2 \left[\frac{m_s}{m_s + \epsilon_k(m_0 - m_s/2)}\right] \left[\frac{m_c}{m_c + \epsilon_k(m_0 - m_c/2)}\right]. \tag{38}$$

Now, consider the ensembles at $\beta = 6.20$, with $m_{u/d} = 0.00125$, $m_s = 0.04$, $m_c = 0.55$ (see Table II), and $m_0 = 1.3$. If a relatively large $\lambda_{\rm min}$ has been used in computing the optimal weights $\{\omega_s\}$ for V_{N_s} such that $\epsilon_k = 0.05$, then (38) gives

$$W^{(2)} \sim \{(1.888 \times 10^{-2})^2 \times 0.3846 \times 0.9148\}^n \sim (1.254 \times 10^{-4})^n \ll 1, \tag{39}$$

where u/d quarks at the physical point plays the dominant role in making $W^{(2)} \ll 1$. On the other hand, if a sufficiently small $\lambda_{\rm min}$ has been used in computing the optimal weights $\{\omega_s\}$ for V_{N_s} such that $\epsilon_k \lesssim 10^{-5}$, Eq. (38) gives

$$W^{(2)} \gtrsim \{(0.98971)^2 \times 0.99968 \times 0.99998\}^n \sim (0.9792)^n. \tag{40}$$

Thus, to make the reweighting method work efficiently, $\lambda_{\rm min}$ is required to be sufficiently small such that $W^{(2)} \sim 1$.

(3) $D_{\rm ov}(0)$ has $n+k$ zero modes ($n \geq 0$, $k \geq 1$), but $D_{N_s}(0)$ only has n zero modes. First, consider the case $k = 1$. Then, $D_{\rm ov}(0)$ has one extra zero mode plus its accompanying nonzero real eigenmode at $2m_0$, in comparison with the real eigenvalues of $D_{N_s}(0)$. Since the total number of eigenvalues must be the same for both $D_{\rm ov}(0)$ and $D_{N_s}(0)$, this implies that $D_{N_s}(0)$ has one extra complex conjugate pair very close to $2m_0$, in comparison with the complex conjugate pairs of $D_{\rm ov}(0)$. This can be visualized as follows. Imagine $D_{N_s}(0)$ approaching $D_{\rm ov}(0)$ by gradually increasing N_s and decreasing $\lambda_{\rm min}$; then, at some point, one of its complex conjugate pairs very close to $2m_0$ transforms into two real eigenmodes, one at zero and the other at $2m_0$. The rest of the complex conjugate pairs remain almost identical for both $D_{\rm ov}(0)$ and $D_{N_s}(0)$. Thus, the weight factor (32) for $N_f = 2+1+1$ QCD is

$$\left(\frac{m_{u/d}}{2m_0}\right)^2 \left(\frac{m_s}{2m_0}\right) \left(\frac{m_c}{2m_0}\right) W^{(2)},$$

which immediately generalizes to $k \geq 1$,

$$W^{(3)} = \left(\frac{m_{u/d}}{2m_0}\right)^{2k} \left(\frac{m_s}{2m_0}\right)^{k} \left(\frac{m_c}{2m_0}\right)^{k} W^{(2)}, \tag{41}$$

where $W^{(2)}$ is given in (38). For the ensembles at $\beta = 6.20$, with quark masses in Table II and $m_0 = 1.3$, Eq. (41) gives

$$W^{(3)} \simeq \left(\frac{0.00125}{2.6}\right)^{2k} \left(\frac{0.04}{2.6}\right)^{k} \left(\frac{0.55}{2.6}\right)^{k}$$
$$W^{(2)} \simeq (7.522 \times 10^{-10})^k W^{(2)} \ll 1.$$

If a significant fraction of the nontrivial configurations in the ensemble have $W^{(3)} \ll 1$, then the reweighting method cannot work efficiently, and the reweighted χ_t (31) is unreliable.

(4) $D_{N_s}(0)$ has $n+k$ zero modes ($n \geq 0$, $k \geq 1$), but $D_{\rm ov}(0)$ only has n zero modes. In principle, this scenario cannot happen since $S_{N_s}(H_w)$ is only an approximation of $H_w/\sqrt{H_w^2}$, especially for the low-lying eigenvalues $0 < |\lambda(H_w)| < \lambda_{\rm min}$. Thus, $D_{N_s}(0)$ cannot have more zero modes than $D_{\rm ov}(0)$.

Note that it is rather challenging to compute the weight factor (32) numerically, since it needs to project the low-lying eigenmodes of both $V_{\rm ov}$ and V_{N_s}. For $V_{\rm ov}$, the projection can be sped up significantly by low-mode preconditioning with a few hundred of low modes of H_w with eigenvalues in the range $0 < |\lambda(H_w)| \le \lambda_u$, where λ_u depends on the gauge configuration and the number of low modes. Then, the sign function $H_w/\sqrt{H_w^2}$ with eigenvalues of $|H_w|$ in the range $[\lambda_u, 6.2]$ is approximated by the Zolotarev optimal rational polynomial with 64 poles and $\lambda_{\rm min}/\lambda_{\rm max} = \lambda_u/6.2$. On the other hand, for the projection of low modes of V_{N_s}, one is not allowed to use the low modes of H_w for preconditioning. Otherwise, the corresponding $D_{N_s}(m_q)$ is not equal to the effective four-dimensional Dirac operator of the optimal DWF action in the HMC simulation. It turns out that the projection of low modes of V_{N_s} is about five to ten times more expensive than that of $V_{\rm ov}$.

Testing with the ensemble of 374 configurations on the $64^3 \times 6$ lattice at $\beta = 6.20$ as described in Sec. V, we project 40 low modes of V_{N_s} for the 78 nontrivial configurations with nonzero overlap index in Table V and find that V_{N_s} does not have any ± 1 real eigenmodes for all of them. Thus, $Q_i = \text{index}\{D_{N_s}(0)\} = 0$, the reweighted χ_t (31) is exactly zero, and the reweighting method fails completely in this case. Next, we change $\lambda_{\rm min}$ from 0.05 to 0.001 and recompute the optimal weights $\{\omega_s\}$ for $S_{N_s}(H_w)$ [see Eq. (13)] and repeat the low-mode projections. Then, we find that $\text{index}\{D_{N_s}(0)\} = \text{index}\{D_{\rm ov}(0)\} = n_+ - n_-$ for all 78 nontrivial configurations, but there are ~20% configurations with weight factor $W < 0.1$. After increasing N_s from 16 to 32 and decreasing $\lambda_{\rm min}$ from 0.001 to 0.00001, then $\text{index}\{D_{N_s}(0)\} = \text{index}\{D_{\rm ov}(0)\} = n_+ - n_-$, and all weight factors are larger than 0.8. This numerical experiment suggests a viable way to perform the optimal DWF simulation such that the resulting gauge configurations are eligible for reweighting to the exact chiral symmetry limit, that is, to use the optimal weights $\{\omega_s\}$ with a sufficiently small $\lambda_{\rm min}$ and a sufficiently large N_s such that V_{N_s} has exactly the same number of ± 1 real eigenmodes as those of $V_{\rm ov}$, and all -1 real eigenvalues have very small deviations with $\epsilon_k < 10^{-5}$. Then, $\text{index}[D_{N_s}(0)] = \text{index}[D_{\rm ov}(0)]$ and the weight factor $W \sim 1$ for all configurations, and the reweighting method works efficiently.

For completeness, we also project the low modes of $V_{N_s} = \gamma_5 S_{N_s}(H_w)$ with $S_{N_s}(H_w)$ in polar approximation, which is equivalent to setting $\omega_s = 1$ in the optimal DWF. We find that the index of $D_{N_s}(0)$ with polar approximation is zero for all 78 nontrivial configurations with nonzero overlap index in Table V, for $N_s \le 128$. This implies that the reweighting method also fails for other variants (e.g., Shamir/Möbius) of DWF with $N_s \le 128$. Note that for Shamir/Möbius DWF the approximate sign function is $S_{N_s}(H)$ with polar approximation, where $H = \gamma_5 D_w (2 + D_w)^{-1}$. For any gauge configuration, the low-lying eigenvalues of H should be close to those of $H_w/2$. Thus, we expect that the $D_{N_s}(0)$ of Shamir/Möbius DWF with $N_s \le 128$ also has zero index for all 78 nontrivial configurations with nonzero overlap index in Table V, even though we have not performed the numerical test. This suggests that the viable way to perform Shamir/Möbius DWF simulation such that the resulting gauge configurations are eligible for reweighting to the exact chiral symmetry limit is to use a sufficiently large N_s which is much larger than that of optimal DWF, since it does not have any parameter like $\lambda_{\rm min}$ to enhance the chiral symmetry for the low-lying eigenvalues of $|H|$.

In the following, we discuss the issue of using the clover charge in the Wilson flow to identify the nontrivial configurations in the reweighting method (31). For nonchiral lattice Dirac operators (e.g, the Wilson Dirac operator, the staggered Dirac operator, etc.), they do not have exact zero modes at finite lattice spacing. Thus, it is impossible to use the eigenvalues of any nonchiral lattice Dirac operator to identify the topologically nontrivial configurations in (31). If the clover charge in the Wilson flow is used to identify the nontrivial configurations, it could be different from the index of the nonchiral lattice Dirac operator in the continuum limit. As demonstrated in Sec. V, for an ensemble of 374 gauge configurations at $T \sim 516$ MeV, even at the Wilson flow time $t/a^2 = 25$ where χ_t measured by round$[Q_{\rm clover}]$ is almost equal to that by the overlap index at $t = 0$, there are more than 72% (57 out of 79) of the configurations with round$[Q_{\rm clover}] \neq 0$ but with the overlap index $(n_+ - n_-) = 0$ at $t = 0$. For a cross-check, one can use the index of overlap operator to identify the nontrivial configurations for reweighting, to check whether the reweighted χ_t in the continuum limit is consistent with that obtained by using the clover charge in the Wilson flow to identify the nontrivial configurations.

VII. COMPARISON WITH OTHER LATTICE STUDIES

In the following, we survey the continuum extrapolated $\chi_t(T)$ in recent lattice studies with $N_f = 2 + 1(+1)$ dynamical fermions at/near the physical point and discuss their discrepancies. In Fig. 6, results of four lattice studies are plotted, while other results not shown are either not in the continuum limit or only a single data point at one temperature, and they will be included in the following discussions. Note that the data points of Bonati *et al.* [19] and Petreczky *et al.* [20] are read off from the figures in the original publications; thus, they may have large uncertainties due to the limited resolution of human eyes.

The results of Bonati *et al.* [19] were obtained from direct simulations of $N_f = 2 + 1$ lattice QCD at the physical point (with $m_\pi = 135$ MeV, and $m_s/m_{ud} = 28.15$), using the

tree-level improved Symanzik gauge action and the stout improved staggered fermion action. The continuum limit of $\chi^{1/4}$ was obtained by extrapolation with three lattice spacings $a = (0.0572, 0.0707, 0.0824)$ fm. The topological charge of each configuration was measured by the clover charge after cooling.

The results of Petreczky *et al.* [20] were obtained from simulations of $N_f = 2+1$ lattice QCD with $m_\pi = 160$ MeV and $m_s/m_{ud} = 20$ (physical m_s), using the tree-level improved gauge action and the highly improved staggered quark action (HISQ). The continuum limit of $\chi_t^{1/4}$ is obtained by extrapolation with three lattice spacings with $N_t = (8, 10, 12)$. They used two methods to measure the topological susceptibility: 1) the clover charge in the Symanzik flow and 2) the chiral susceptibilities χ_π and χ_δ and the relation $\chi_t = m_{ud}^2 \chi_{\rm disc}$ for $T > T_c$. Both methods gave compatible results. In Fig. 6, only the data points obtained with the clover charge are plotted.

The topological susceptibility of Borsanyi *et al.* [21] was measured by the clover charge in the Wilson flow, and the data points in Fig. 6 are based on the numerical results in Table S9 of the Supplementary Information of Ref. [21], which are supposed to be the continuum extrapolated topological susceptibility of $N_f = 2+1+1$ QCD at the physical point, plus the theoretically estimated contribution of the b quark and the correction for the mass difference between u and d quarks. However, only seven data points in the range of $T = 130$–300 MeV were based on direct simulations of $N_f = 2+1+1$ lattice QCD at the physical point, using the tree-level Symanzik gauge action and the staggered quark action with four levels of stout smearing. For other data points, they were obtained by the fixed sector integral and the eigenvalue reweighting techniques from three sets of unphysical simulations:

(a) $N_f = 3+1$ (three flavors of physical m_s and one flavor of physical m_c) for $T = 150$–500 MeV;
(b) same as (a) but at fixed topology for $T = 300$–3000 MeV;
(c) $N_f = 2+1$ overlap fermions at fixed topology for three temperatures, $T = (300, 450, 650)$ MeV, and each for six m_{ud} quark masses between physical m_s and physical $m_{ud}^{\rm phys}$.

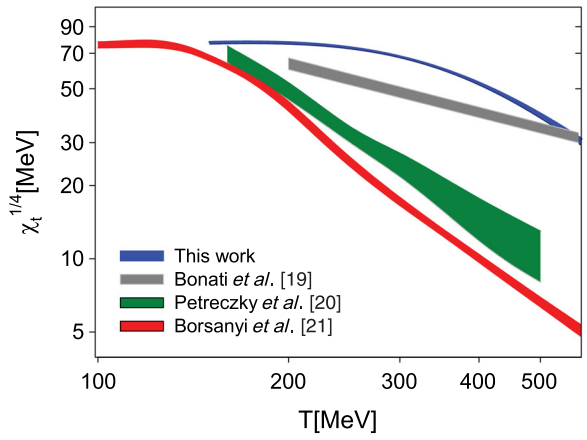

FIG. 6. Comparison of the continuum extrapolated fourth-root topological susceptibility $\chi_t^{1/4}(T)$ for four lattice studies.

Thus, for comparison with other lattice results, we focus on their data points in the range of $T = 150$–300 MeV, which were obtained by direct simulations at the physical point, corrected by the eigenvalue reweighting, and extrapolated to the continuum limit.

First, we compare the results of Bonati *et al.* [19], Petreczky *et al.* [20], and Borsanyi *et al.* [21]. Evidently, the discrepancies between Petreczky *et al.* and Borsanyi *et al.* are much smaller than those between Bonati *et al.* and Borsanyi *et al.* Moreover, after the results of Petreczky *et al.* [20] are transformed from $m_\pi = 160$ MeV to the physical point by the relation $\chi_t^{1/4} \propto m_\pi$, they seem to be in good agreement with the results of Borsanyi *et al.* [21].

In a more recent study by Bonati *et al.* [49] in $N_f = 2+1$ lattice QCD at the physical point with tree-level improved Symanzik gauge action and the stout improved staggered fermion action, using the multicanonical algorithm (to enhance the topological fluctuations), they obtained the continuum extrapolated $\chi_t^{1/4} = (3 \pm 3 \pm 2)$ MeV at $T \simeq 430$ MeV, which is $\sim 9\sigma$ different from their previous result $\sim 38(2)$ MeV in Ref. [19]. The topological charge of each configuration is measured by the clover charge after cooling. Then, in the most recent study of the same group [50], using the same set of ensembles at $T \simeq 430$ MeV [49], they obtained the continuum extrapolated $\chi_t^{1/4} \sim 20(3)$ MeV (read off from Fig. 2 of Ref. [50]), which is $\sim 5\sigma$ different from their 2018 result [49] and $\sim 3\sigma$ different from 9(1) MeV of Borsanyi *et al.* [21]. Note that in Ref. [50] two methods had been used to measure the χ_t: 1) the index of the staggered spectral projector and 2) the clover charge after cooling. Both methods gave compatible results.

In Table VI, we compile all results of continuum extrapolated $\chi_t^{1/4}$ at $T \simeq 430$ MeV, together with their lattice actions, simulation methods and techniques, and methods (gluonic and fermionic ones) for χ_t measurement.

We note that there are ongoing studies of $\chi_t(T)$ in $N_f = 2+1+1$ lattice QCD with Wilson twisted mass fermions [22,51]. Using the relation $\chi_t = m_{ud}^2 \chi_{\rm disc}$ to measure χ_t via the noise estimation of the disconnected chiral susceptibility of u/d quarks, they obtained $\chi_t^{1/4} \sim 10(2)$ MeV at $T \simeq 430$ MeV, with $m_\pi = 210$ MeV and $a \sim 0.065$ fm [22]. Their recent results at the physical point with $m_\pi = 139(1)$ MeV and $a \sim 0.080$ fm were presented in Ref. [51] and at $T \simeq 430$ MeV, $\chi_t^{1/4} \sim 4(1)$ MeV (read off from Fig. 2 of Ref. [51]). This implies that the continuum extrapolated $\chi^{1/4}$ at $T \simeq 430$ MeV would be less than 4(1) MeV. This is added to Table VI for comparison with other continuum extrapolated $\chi_t^{1/4}$ at the same temperature.

TABLE VI. The continuum extrapolated fourth root of the topological susceptibility $\chi_t^{1/4}$ [MeV] at $T \simeq 430$ MeV. The abbreviations are DWF, HISQ, SISF (stout-improved staggered fermion), WTMF (Wilson twisted mass fermion); Wilson (Wilson plaquette action), Symanzik (tree-level improved Symanzik gauge action), Iwasaki (Iwasaki gauge action with $c_0 = 3.648$ and $c_1 = -0.331$); REW (eigenvalue reweighting technique), FSI (fixed sector integral technique), MCA (multicanonical algorithm); CCC (clover charge after cooling), CSF (clover charge in the Symanzik flow), CWF (clover charge in the Wilson flow), DIS (use $\chi_t = m_{ud}^2 \chi_{\rm disc}$), SSP (staggered spectral projectors).

Reference	Quark	Gluon	N_f	m_π [MeV]	Simulation	Measurement	$\chi_t^{1/4}$ (MeV)
Bonati *et al.* [19]	SISF	Symanzik	$2+1$	135	Direct	CCC	38(2)
Petreczky *et al.* [20]	HISQ	Symanzik	$2+1$	160	Direct	CSF, DIS	15(2), 10(3)
Borsanyi *et al.* [21]	SISF	Symanzik	$2+1+1$	140	REW, FSI	CWF	9(1)
Bonati *et al.* [49]	SISF	Symanzik	$2+1$	140	Direct + MCA	CCC	3(3)(2)
Athenodorou *et al.* [50]	SISF	Symanzik	$2+1$	140	Direct + MCA	CCC, SSP	18(3), 20(3)
Kotov *et al.* [51]	WTMF	Iwasaki	$2+1+1$	140	Direct	DIS	$< 4(1)$
This work	DWF	Wilson	$2+1+1$	140	Direct	CWF	48(1)

The discrepancies of the continuum extrapolated $\chi_t^{1/4}$ shown in Fig. 6 and in the last column of Table VI suggest that the systematic errors in all/most lattice studies have not been under control. Note that, except for the work of Borsanyi *et al.* [21], no lattice results have been corrected for the cutoff effects due to the lattice Dirac operator in a nontrivial gauge background not possessing (or not having the complete set of) exact zero modes. That is, such cutoff effects of the lattice Dirac operator were corrected at finite lattice spacing before extrapolating $\chi_t(a, T)$ to the continuum limit. Otherwise, the results of $\chi_t(T)$ in the continuum will be suffered from large cutoff effects. Now, the question is what would be the scenario if all lattice results were corrected for these cutoff effects. Since there were four studies using the stout-improved staggered fermions and one of them has already performed the reweighting [21], we can use the effective reweighting factors obtained in Ref. [21] to get a rough estimate of the reweighted $\chi_t^{1/4}$ in the other three studies [19,49,50].

According to the data in Table S8 and Fig. 25 of the Supplementary Information and the Extended Data Fig. 4 in Ref. [21], the reweighting at $T = 300$ MeV effectively imposes a factor ~0.38 to the continuum extrapolated $\chi_t^{1/4}$. Note that the reweighting factor for lattice QCD with $N_f = 2+1+1$ staggered fermions is almost the same as that for lattice QCD with $N_f = 2+1$ staggered fermions, since the mass of the charm quark is much larger than the eigenvalue of the would-be zero mode of the massless staggered fermion operator. That is, the reweighting factor of the staggered charm quark is

$$\prod_{i=1}^{2|Q_t|} \left(\frac{m_c^2}{m_c^2 + |\lambda_i|^2} \right)^{1/4} \simeq 1, \qquad m_c \gg |\lambda_i|.$$

Thus, the same effective reweighting factor ~0.38 can be used for a rough estimate of the reweighted $\chi_t^{1/4}$ at $T = 300$ MeV in another $N_f = 2+1$ lattice QCD study with stout-improved staggered fermions. In the case of Ref. [19], it changes the value of $\chi_t^{1/4}$ from ~50(2) MeV to ~19(2) MeV, bringing it into good agreement with the value 17(1) MeV of Borsanyi *et al.* [21].

Next, we turn to the results of $\chi_t^{1/4}$ in Table VI. However, for $T = 430$ MeV, the effective reweighting factor for $N_f = 2+1+1$ stout-improved staggered fermions is not available in Ref. [21], since the simulation at $T = 430$ MeV was only performed for unphysical $N_f = 3+1$ lattice QCD. Nevertheless, it must be smaller than the value 0.38 at $T = 300$ MeV, since the eigenvalue of the would-be zero mode becomes larger at higher T. For a very rough estimate, we take it to be 0.35 at $T = 430$ MeV and apply it to the entries of Refs. [19,49,50] in the last column of Table VI. This gives the "reweighted" $\chi_t^{1/4}$: 13(1) MeV for Ref. [19], 2(2)(1) MeV for Ref. [49], and $\{6(2), 7(2)\}$ MeV for [50]. Thus, after such a reweighting at $T \simeq 430$ MeV, Bonati *et al.* [19] and Athenodorou *et al.* [50] come in closer agreement with Borsanyi *et al.* [21], while Bonati *et al.* [49] are in greater disagreement with Borsanyi *et al.* [21].

For a lattice fermion operator different from the stout-improved staggered fermion operator, the effective reweighting factor obtained in Ref. [21] cannot be used for a rough estimate of the reweighted $\chi_t^{1/4}$, since their cutoff effects could be very different. In general, for any lattice Dirac operator (except the overlap operator), the reweighted $\chi_t(T)$ would be smaller than that without reweighting, and the reduction becomes larger at higher T. This suggests that the continuum extrapolated $\chi_t(T)$ of all lattice studies could be brought into agreement if the cutoff effects of the lattice Dirac operators would be corrected.

Recall that the reweighting method deforms the path integral nonlocally; in principle, it is not guaranteed to give the correct result. Moreover, the reweighting method becomes inefficient if the weights have large fluctuations. Thus, it is necessary to cross-check the results

of Borsanyi *et al.* [21] by direct simulations with overlap fermions.

For DWFs, the viable way to reduce the cutoff effects is to perform simulations with more and more precise chiral symmetry successively. On the other hand, if one resorts to reweighting, the prerequisite for a reliable reweighting is that the chiral symmetry of the DWF should be sufficiently precise such that for any nontrivial gauge background its effective four-dimensional Dirac operator possesses the same number of exact zero modes as the overlap operator, as discussed in Sec. VI.

About the results of continuum extrapolated $\chi_t^{1/4}(T)$ in this work, they are the largest among all lattice results at the same temperature. Theoretically, they would become smaller in the exact chiral symmetry limit (with $N_s \to \infty$ and $\lambda_{\rm min} \to 0$). At this moment, we do not know to what extent the decrease would be and whether they would agree with the results of Borsanyi *et al.* [21]. Note that we have used the Wilson plaquette action and the optimal DWF operator with thin links, unlike other lattice studies using improved gauge actions and the stout-improved lattice Dirac operator. Thus, the topological fluctuations (and the susceptibility) in our case are expected to be larger than those using other actions at the same temperature and lattice spacing. It is unclear to what extent the cutoff effects due to the gauge action and the link variables entering the lattice Dirac operator could affect the continuum extrapolated $\chi_t(T)$, even though in principle all cutoff effects are supposed to vanish in the continuum limit. On the other hand, it is also unclear whether using improved gauge actions and improved lattice Dirac operators with fat links would suppress the topological fluctuations too much such that the continuum extrapolation would be distorted. Further studies are required to answer these questions.

Other systematics in Ref. [21] are the fixed-sector integral method (in T) together with the reweighting method to extend the unphysical $N_f = 3 + 1$ simulations from 500 to 3000 MeV and also the integral method (in m_{ud}) to bring the unphysical $N_f = 3 + 1$ results from $m_{ud} = m_s^{\rm phys}$ to physical $m_{ud}^{\rm phys}$. These systematics can be cross-checked by direct simulations with $N_f = 2 + 1 + 1$ overlap fermions at the physical point and without fixing topology. Since direct simulations of overlap fermions at the physical point is prohibitively expensive; a viable alternative is to use the optimal DWF with sufficiently small $\lambda_{\rm min}$ and sufficiently large N_s, which may be feasible with the exaflop machines.

To conclude this section, we reiterate that the systematic errors of all/most lattice results of $\chi_t(T)$ have not been under control, leading to the discrepancies as shown in Fig. 6 and in Table VI. Moreover, any convergence of several lattice results at some temperature does not necessarily imply that it would be the correct physical/theoretical value, which can be established only after the systematic errors of all these lattice results have been corrected.

VIII. CONCLUDING REMARKS

To determine the topological susceptibility of finite temperature QCD is a very challenging task. So far, all lattice studies have not obtained satisfactory results with all systematic errors under control, at the physical point as well as in the continuum limit, for $T > T_c$.

The present study is the first attempt to simulate finite temperature lattice QCD with $N_f = 2 + 1 + 1$ domain-wall quarks at the physical point. We perform the HMC simulation of lattice QCD with $N_f = 2 + 1 + 1$ optimal domain-wall quarks at the physical point, on the $64^3 \times (64, 20, 16, 12, 10, 8, 6)$ lattices, each with three lattice spacings $a \sim (0.064, 0.068, 0.075)$ fm. The chiral symmetry in the HMC simulation is preserved with $N_s = 16$ in the fifth dimension, and the optimal weights $\{\omega_s, s = 1, \ldots, 16\}$ are computed with $\lambda_{\rm min} = 0.05$ and $\lambda_{\rm max} = 6.2$, with the error of the sign function of H_w less than 1.2×10^{-5}, for eigenvalues of H_w satisfying $\lambda_{\rm min} \le |\lambda(H_w)| \le \lambda_{\rm max}$. The residual masses of $(u/d, s, c)$ quarks are less than $(0.09, 0.08, 0.04)$ MeV$/c^2$, respectively (see Table I). The bare quark masses and lattice spacings are determined on the 64^4 lattices (see Table II). For each lattice spacing, the bare quark masses of u/d, s, and c are tuned such that the lowest-lying masses of the meson operators $\{\bar{u}\gamma_5 d, \bar{s}\gamma_i s, \bar{c}\gamma_i c\}$ are in good agreement with the physical masses of $\{\pi^{\pm}(140), \phi(1020), J/\psi(3097)\}$, respectively.

In this paper, we determine the topological susceptibility for $T > T_c$. The topological charge of each gauge configuration is measured by the clover charge in Wilson flow at the flow time $t = 0.8192$ fm^2, where the topological susceptibility of any gauge ensemble attains its plateau. Using the topological susceptibility $\chi_t(a, T)$ of 15 gauge ensembles with three different lattice spacings and different temperatures in the range $T \sim 155$–516 MeV (see Table III), we fit the data points to the ansatz (26) and obtain the fitted parameters and $\chi_t(T)$ in the continuum limit (see Fig. 2). In the limit $T \gg T_c$, it gives $\chi_t(T) = 12.8(1)(T_c/T)^{8.1(2)}$ (in units of fm^{-4}), which agrees with the temperature dependence of $\chi_t(T)$ in the DIGA [15], $\chi_t(T) \sim T^{-8.3}$ for $N_f = 4$. This implies that our data points of $\chi_t(a, T)$ for $T > 350$ MeV are valid, up to an overall constant factor.

To investigate the volume dependence of topological susceptibility, we generate another set of ensembles of lattice sizes $32^3 \times (16, 12, 10, 8, 6)$, with lattice spacing $a \sim 0.0641$ fm and volume $\sim(2.053$ fm$)^3$, and obtain the $\chi_t(a, T)$ for $T \sim 192$–512 MeV (see Table IV). Comparing the topological susceptibilities of this relatively smaller volume with their counterparts of a larger volume $\sim(4.074$ fm$)^3$ on the $64^3 \times (16, 12, 10, 8, 6)$ lattices with

lattice spacing $a \sim 0.0636$ fm in Table III and also with those in the infinite volume limit by extrapolation (see Fig. 3), we conclude that the values of $\chi_t^{1/4}$ in Table III do not suffer from significant finite-volume systematics.

Since our present simulation is not at the exact chiral symmetry limit, we investigate the feasibility of using the reweighting method to obtain χ_t in the exact chiral symmetry limit. In Sec. VI, we give a detailed discussion of the reweighting method for DWF. We find that the prerequisite for the reweighting method to work efficiently for DWF is that the index of the effective four-dimensional Dirac operator $D_{N_s}(0)$ [see Eq. (13)] of the DWF is equal to the index of the overlap Dirac operator $D_{\rm ov}(0)$ for each configuration in the ensemble. Moreover, the approximate sign function $S_{N_s}(H)$ is required to be sufficiently precise, especially for the low-lying eigenvalues of $|H|$ (where $H = H_w = \gamma_5 D_w$ for optimal DWF and $H = \gamma_5 D_w(2 + D_w)^{-1}$ for Shamir/Möbius DWF). Then, the weight factor (32) of each configuration is of the order 1, i.e., $W_i \sim 1$. To fulfill above requirements, for optimal DWF simulation, it has to use a sufficiently small $\lambda_{\rm min}$ and also a sufficiently large N_s, while for the Shamir/Möbius DWF simulation, it needs to use some N_s much larger than that of optimal DWF, since it does not have any parameter like $\lambda_{\rm min}$ to enhance the chiral symmetry for the low-lying eigenvalues of $|H|$.

The above approach of obtaining $\chi_t(T)$ in the exact chiral symmetry limit is to reweight $\chi_t(a,T)$ to ${\chi_t}^{\rm ov}(a,T)$ at finite lattice spacing a and temperature T, then use a set of data points of ${\chi_t}^{\rm ov}(a,T)$ at many different a and T to extract ${\chi_t}^{\rm ov}(T)$ in the continuum limit for any T. Nevertheless, this rigorous approach seems to be prohibitively expensive. Besides the very expensive DWF simulation with $\lambda_{\rm min} \lesssim 0.00001$ and $N_s \gtrsim 32$, there are even more costly projections of low modes of V_{N_s} and $V_{\rm ov}$ for computing the weight factor of each configuration in the ensembles. Pursuing this approach is out of the question unless the exaflop computers are available. Nevertheless, from the viewpoint of universality, even ${\chi_t}^{\rm DWF}(a,T)$ [measured by the index of $D_{N_s}(0)$] at finite lattice spacing is different from ${\chi_t}^{\rm ov}(a,T)$; theoretically, in the continuum limit, both ${\chi_t}^{\rm DWF}(T)$ and ${\chi_t}^{\rm ov}(T)$ should go to the same universal value, since both $D_{N_s}(0)$ and $D_{\rm ov}(0)$ go to the massless Dirac operator in the continuum limit, provided that the chiral symmetry of DWF is sufficiently precise such that $\text{index}\{D_{N_s}(0)\} = \text{index}\{D_{\rm ov}(0)\}$. Then, the reweighting at finite lattice spacing seems to be unnecessary. Moreover, for an ensemble generated by DWF simulation with effective four-dimensional Dirac operator $D_{N_s}(0)$ sufficiently close to $D_{\rm ov}(0)$, the topological charge of each configuration can be measured by $Q_{\rm clover}$ in the Wilson flow, since it is expected that $\chi_t(\text{clover}) = \chi_t(\text{overlap})$ in the continuum limit and in the infinite volume limit. Further studies are required to examine whether any of the above scenarios could be realized in practice.

ACKNOWLEDGMENTS

We are grateful to Academia Sinica Grid Computing Center (ASGC) and National Center for High Performance Computing (NCHC) for the computer time and facilities. This work is supported by the Ministry of Science and Technology (Grants No. 108-2112-M-003-005, No. 109-2112-M-003-006, and No. 110-2112-M-003-009).

APPENDIX: RENORMALIZED CHIRAL CONDENSATE

As discussed in Sec. I, the chiral condensate Σ is the order parameter of spontaneously chiral symmetry breaking in QCD. At low temperatures ($T < T_c$), the chiral symmetry of QCD is spontaneously broken, and the ChPT gives the relation between the chiral condensate and the topological susceptibility. However, at high temperatures ($T > T_c$), the chiral symmetry of u and d quarks is effectively restored, and the chiral condensate vanishes. Thus, the ChPT becomes inapplicable for $T > T_c$, and it cannot give an expression of $\chi_t(T)$. Theoretically, the topological susceptibility can be nonzero for $T > T_c$ due to the quantum fluctuations of the physical (u, d, s, c, b) quarks with nonzero masses. Even though the chiral condensate $\Sigma(T)$ seems to be irrelevant to $\chi_t(T)$ for $T > T_c$, it is important to find out how the chiral condensate $\Sigma(T)$ changes with respect to T, and from which to determine the pseudocritical temperature T_c, and to understand the nature of the chiral symmetry restoration. To this end, lattice QCD provides a viable framework for nonperturbative determination of $\Sigma(T)$ from the first principles.

In lattice QCD, the quark condensate $\Sigma(m_q, T)$ suffers from the quadratic divergences in the continuum limit. To remove the quadratic divergences of the u/d quark condensate, one considers the subtracted quark condensate

$$\Delta_{us}(T) = \Sigma(m_u, T) - \frac{m_u}{m_s}\Sigma(m_s, T), \tag{A1}$$

where m_u and m_s are the bare masses of the u and s quarks. Moreover, the multiplicative renormalization factor in (A1) can be eliminated by normalization with its corresponding value at $T = 0$, i.e.,

$$\Delta^R_{us}(T) = \frac{\Sigma(m_u, T) - \frac{m_u}{m_s}\Sigma(m_s, T)}{\Sigma(m_u, 0) - \frac{m_u}{m_s}\Sigma(m_s, 0)}, \tag{A2}$$

which is called the renormalized chiral condensate [52].

In the following, we present our first results of $\Delta^R_{us}(T)$ for $T \simeq 131$–516 MeV, in lattice QCD with $N_f = 2 + 1 + 1$ domain-wall quarks at the physical point, for the 14 ensembles listed in Table VII. There are 12 ensembles

TABLE VII. The renormalized chiral condensate $\Delta^R_{us}(T)$ of 14 gauge ensembles.

β	a (fm)	N_x	N_t	T (MeV)	$N_{\rm confs}$	$\Delta^R_{us}(T)$
6.15	0.0748	64	20	131	152	0.594(63)
6.18	0.0685	64	20	144	182	0.299(34)
6.20	0.0636	64	20	155	218	0.133(16)
6.20	0.0636	64	16	193	395	0.040(8)
6.18	0.0685	64	12	240	194	0.015(1)
6.15	0.0748	64	10	263	274	0.010(1)
6.18	0.0685	64	10	288	263	$6.58(33)\times10^{-3}$
6.20	0.0636	64	10	310	243	$2.29(62)\times10^{-3}$
6.15	0.0748	64	8	329	323	$4.43(16)\times10^{-3}$
6.18	0.0685	64	8	360	365	$3.39(14)\times10^{-3}$
6.20	0.0636	64	8	387	317	$2.24(72)\times10^{-3}$
6.15	0.0748	64	6	438	303	$2.43(1.26)\times10^{-3}$
6.18	0.0685	64	6	479	382	$0.76(2.42)\times10^{-3}$
6.20	0.0636	64	6	516	732	$8.27(56)\times10^{-4}$

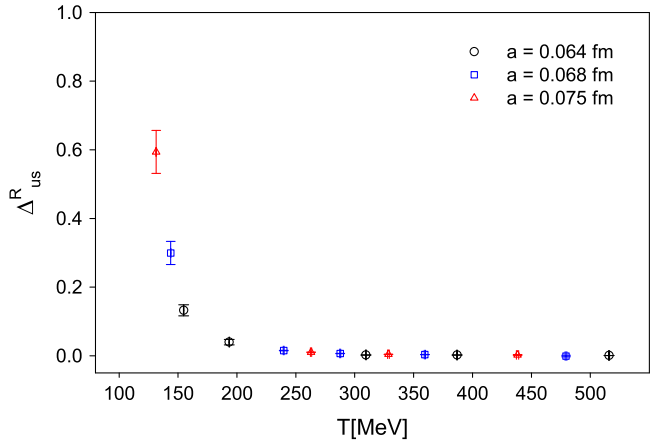

FIG. 7. The renormalized chiral condensate Δ^R_{us} vs the temperature T.

with $T > 150$ MeV (a subset of the ensembles in Table III) and two ensembles with $T < 150$ MeV. The quark condensate $\Sigma(m_q, T) = \mathrm{Tr}(D_c + m_q)^{-1}/V$ is estimated by the noise method, using 24–240 Z_2 noise vectors to evaluate the all-to-all quark propagators for each configuration. The number of configurations of each ensemble for the evaluation of $\Delta^R_{us}(T)$ is given in the column $N_{\rm confs}$. The data of $\Delta^R_{us}(T)$ in the last column are plotted versus T in Fig. 7. Here, the normalization factors [i.e., the denominator in (A2)] for three different lattice spacings are evaluated on the 64^4 lattices with (100, 67, 84) configurations for $\beta = (6.20, 6.18, 6.15)$, respectively.

Comparing the data of Δ^R_{us} in Fig. 7 with its counterpart in $N_f = 2+1+1$ QCD with maximally twisted mass Wilson fermions at $m_\pi = 210$ MeV (see Fig. 3 in Ref. [22]), we find that the trends of the falling of $\Delta^R_{us}(T)$ (as T is increased from low to high temperatures) are consistent with each other. However, the fastest falling of $\Delta^R_{us}(T)$ in Fig. 7 is in the range of $T \sim 145$–150 MeV, while it is ~161–165 MeV in Ref. [22]. Moreover, $\Delta^R_{us}(T)$ in Fig. 7 falls more steeply than its counterpart in Ref. [22]. The discrepancies can be attributed to the different parameters in these two studies, namely, the unphysical $m_\pi = 210$ MeV and a smaller volume $\sim(3.1\ \mathrm{fm})^3$ in Ref. [22], versus the physical $m_\pi = 140$ MeV and a larger volume $\sim(4.1\ \mathrm{fm})^3$ in this study. In general, as m_π gets smaller, the pseudocritical temperature T_c becomes lower, the range of T for the fastest falling of $\Delta^R_{us}(T)$ becomes narrower, and the falling becomes steeper. Furthermore, these effects are enhanced as the volume gets larger.

Comparing the data of Δ^R_{us} in Fig. 7 with its counterpart in $N_f = 2+1$ QCD with staggered fermions at the physical point and in the continuum limit [53,54], we find that the fastest falling of $\Delta^R_{us}(T)$ in $N_f = 2+1$ QCD is in the range of $T \sim 155$–165 MeV, while it is ~145–150 MeV in this study. This seems to suggest that the pseudocritical temperature in $N_f = 2+1$ QCD is $T_c \sim$ 155–160 MeV, higher than that ($T_c \sim 145$–150 MeV) in $N_f = 2+1+1$ QCD. Note that the ratio $(m_{ud}/m_s)^{\rm phys}$ (the physical point) was set to ~0.0355 in Ref. [53] and was extrapolated to 0.037 in Ref. [54], which are larger than the $(m_{ud}/m_s)^{\rm phys}$ values ~0.0310–0.03125 (see Table II) in this study. The difference of the ratios of $(m_{ud}/m_s)^{\rm phys}$ between the $N_f = 2+1$ QCD in Refs. [53,54] and the $N_f = 2+1+1$ QCD in this study may shed light on the question as to why T_c in $N_f = 2+1+1$ QCD is lower than that in $N_f = 2+1$ QCD. We will return to this question after more data points around T_c become available and a more precise determination of T_c becomes feasible.

To determine the pseudocritical temperature T_c requires many data points of $\Delta^R_{us}(T)$ in the vicinity of T_c, which is very challenging and beyond the scope of this paper. Note that the HMC simulations of the ensembles at $T < 150$ MeV for $N_f = 2+1+1$ lattice QCD with domain-wall quarks at the physical point are almost prohibitively expensive for us. Moreover, to get a good estimate of the all-to-all quark propagators by the noise method, it is necessary to use a sufficiently large number of noise vectors, which turns out to be very computationally intensive and requires a large amount of disk space. Here, we only measure the renormalized chiral condensate of 14 ensembles for $T \sim 130$–516 MeV and see how it decreases to zero as T is increased. One thing for sure is that all data points of $\chi_t^{1/4}(a, T)$ in Table III are in the chirally symmetric phase.

[1] H. Leutwyler and A. V. Smilga, Phys. Rev. D **46**, 5607 (1992).
[2] G. 't Hooft, Phys. Rev. Lett. **37**, 8 (1976); Phys. Rev. D **14**, 3432 (1976); **18**, 2199(E) (1978).
[3] E. Witten, Nucl. Phys. **B156**, 269 (1979).
[4] G. Veneziano, Nucl. Phys. **B159**, 213 (1979).
[5] J. Gasser and H. Leutwyler, Phys. Lett. B **184**, 83 (1987).
[6] J. Gasser and H. Leutwyler, Phys. Lett. B **188**, 477 (1987).
[7] P. Gerber and H. Leutwyler, Nucl. Phys. **B321**, 387 (1989).
[8] F. C. Hansen and H. Leutwyler, Nucl. Phys. **B350**, 201 (1991).
[9] R. D. Peccei and H. R. Quinn, Phys. Rev. Lett. **38**, 1440 (1977); Phys. Rev. D **16**, 1791 (1977).
[10] S. Weinberg, Phys. Rev. Lett. **40**, 223 (1978).
[11] F. Wilczek, Phys. Rev. Lett. **40**, 279 (1978).
[12] M. Dine, W. Fischler, and M. Srednicki, Phys. Lett. **104B**, 199 (1981).
[13] J. Preskill, M. B. Wise, and F. Wilczek, Phys. Lett. **120B**, 127 (1983).
[14] L. F. Abbott and P. Sikivie, Phys. Lett. **120B**, 133 (1983).
[15] D. J. Gross, R. D. Pisarski, and L. G. Yaffe, Rev. Mod. Phys. **53**, 43 (1981).
[16] E. Berkowitz, M. I. Buchoff, and E. Rinaldi, Phys. Rev. D **92**, 034507 (2015).
[17] R. Kitano and N. Yamada, J. High Energy Phys. 10 (2015) 136.
[18] S. Borsanyi, M. Dierigl, Z. Fodor, S. D. Katz, S. W. Mages, D. Nogradi, J. Redondo, A. Ringwald, and K. K. Szabo, Phys. Lett. B **752**, 175 (2016).
[19] C. Bonati, M. D'Elia, M. Mariti, G. Martinelli, M. Mesiti, F. Negro, F. Sanfilippo, and G. Villadoro, J. High Energy Phys. 03 (2016) 155.
[20] P. Petreczky, H. P. Schadler, and S. Sharma, Phys. Lett. B **762**, 498 (2016).
[21] S. Borsanyi, Z. Fodor, J. Guenther, K. H. Kampert, S. D. Katz, T. Kawanai, T. G. Kovacs, S. W. Mages, A. Pasztor, F. Pittler *et al.*, Nature (London) **539**, 69 (2016) and the Supplementary Information. arXiv:1606.07494; note that the labeling of figures and tables in the preprint is not exactly identical with that in the published paper and the Supplementary Information, and here we always refer to the latter.
[22] F. Burger, E. M. Ilgenfritz, M. P. Lombardo, and A. Trunin, Phys. Rev. D **98**, 094501 (2018).
[23] G. D. Moore, EPJ Web Conf. **175**, 01009 (2018).
[24] M. P. Lombardo and A. Trunin, Int. J. Mod. Phys. A **35**, 2030010 (2020).
[25] T. W. Chiu, Y. C. Chen, and T. H. Hsieh, Proc. Sci., LATTICE2021 (**2022**) 574 [arXiv:2112.02266].
[26] Y. C. Chen and T. W. Chiu (TWQCD Collaboration), Phys. Lett. B **767**, 193 (2017).
[27] T. W. Chiu (TWQCD Collaboration), Proc. Sci., LATTICE2018 (**2018**) 040.
[28] T. W. Chiu (TWQCD Collaboration), Proc. Sci., LATTICE2019 (**2020**) 133 [arXiv:2002.06126].
[29] K. G. Wilson, Phys. Rev. D **10**, 2445 (1974).
[30] T. W. Chiu, Phys. Rev. Lett. **90**, 071601 (2003).
[31] T. W. Chiu, Phys. Rev. D **102**, 034510 (2020).
[32] H. Neuberger, Phys. Lett. B **417**, 141 (1998).
[33] P. H. Ginsparg and K. G. Wilson, Phys. Rev. D **25**, 2649 (1982).
[34] Y. C. Chen and T. W. Chiu (TWQCD Collaboration), Phys. Lett. B **738**, 55 (2014).
[35] T. W. Chiu, Phys. Lett. B **744**, 95 (2015).
[36] T. W. Chiu, T. H. Hsieh, and Y. Y. Mao (TWQCD Collaboration), Phys. Lett. B **717**, 420 (2012).
[37] Y. C. Chen and T. W. Chiu, Phys. Rev. D **100**, 054513 (2019).
[38] M. Hasenbusch, Phys. Lett. B **519**, 177 (2001).
[39] I. P. Omelyan, I. M. Mryglod, and R. Folk, Phys. Rev. Lett. **86**, 898 (2001).
[40] J. C. Sexton and D. H. Weingarten, Nucl. Phys. **B380**, 665 (1992).
[41] R. Narayanan and H. Neuberger, J. High Energy Phys. 03 (2006) 064.
[42] M. Luscher, J. High Energy Phys. 08 (2010) 071; 03 (2014) 092(E).
[43] A. Bazavov *et al.* (MILC Collaboration), Phys. Rev. D **93**, 094510 (2016).
[44] T. W. Chiu *et al.* (TWQCD Collaboration), Proc. Sci., LATTICE2010 (**2010**) 030 [arXiv:1101.0423].
[45] Y. C. Chen and T. W. Chiu (TWQCD Collaboration), Phys. Rev. D **86**, 094508 (2012).
[46] T. W. Chiu and T. H. Hsieh (TWQCD Collaboration), Proc. Sci., IWCSE2013 (**2014**) 058 [arXiv:1412.2505].
[47] T. W. Chiu and T. H. Hsieh, arXiv:1908.01676.
[48] T. W. Chiu, Phys. Rev. D **58**, 074511 (1998).
[49] C. Bonati, M. D'Elia, G. Martinelli, F. Negro, F. Sanfilippo, and A. Todaro, J. High Energy Phys. 11 (2018) 170.
[50] A. Athenodorou, C. Bonanno, C. Bonati, G. Clemente, F. D'Angelo, M. D'Elia, L. Maio, G. Martinelli, F. Sanfilippo, and A. Todaro, Proc. Sci., LATTICE2021 (**2022**) 166 [arXiv:2112.02982].
[51] A. Y. Kotov, A. Trunin, and M. P. Lombardo, Proc. Sci., LATTICE2021 (**2022**) 032 [arXiv:2111.15421].
[52] M. Cheng, N. H. Christ, S. Datta, J. van der Heide, C. Jung, F. Karsch, O. Kaczmarek, E. Laermann, R. D. Mawhinney, C. Miao *et al.*, Phys. Rev. D **77**, 014511 (2008).
[53] S. Borsanyi, Z. Fodor, C. Hoelbling, S. D. Katz, S. Krieg, C. Ratti, and K. K. Szabó (Wuppertal-Budapest Collaboration), J. High Energy Phys. 09 (2010) 073.
[54] A. Bazavov, T. Bhattacharya, M. Cheng, C. DeTar, H. T. Ding, S. Gottlieb, R. Gupta, P. Hegde, U. M. Heller, F. Karsch *et al.*, Phys. Rev. D **85**, 054503 (2012).